Visible-light induced photocatalytic degradation of estrone (E1) with hexagonal copper selenide nanoflakes in water

Saima Farooq [a,b], Rongsheng Cai [c], James McGettrick [d], Emmanuel Pean [d], Matthew Davies [d,e], Ahmed S. Al Harrasi [f], Richard Palmer [c], Chedly Tizaoui [a,*]

[a] Water and Resources Recovery Research Lab, Department of Chemical Engineering, Faculty of Science and Engineering, Swansea University, Swansea, UK
[b] Department of Biological Sciences & Chemistry, College of Arts and Sciences, University of Nizwa, Nizwa, Oman
[c] Nanomaterials Lab, Mechanical Engineering, Faculty of Science and Engineering, Swansea University, Swansea, UK
[d] SPECIFIC IKC, Materials Science and Engineering, Faculty of Science and Engineering, Swansea University, UK
[e] School of Chemistry and Physics, University of KwaZulu-Natal, Durban, South Africa
[f] Natural and Medical Sciences Research Centre, University of Nizwa, Nizwa, Oman

ARTICLE INFO

ABSTRACT

Steroid hormones, being potent endocrine-disruptors, are a menace to human health and aquatic life. Herein, visible-light induced photocatalytic degradation of estrone (E1) by hexagonal copper selenide (CuSe) nanoflakes has been reported. CuSe was synthesised by a facile and low-temperature (100 ^{o}C) co-precipitation method and was characterised. The nanocrystals were of stoichiometric Cu:Se ratio with Se^{2-} and Cu in the $+1/+2$ mixed-valence state and exhibited laminar, flake-like morphology with a preferred hexagonal close-packed structure (P63/mmc) having average particle size and thickness of 0.229 ± 0.146 μm and 0.05 ± 0.02 μm, respectively. The adsorption isotherms of E1 were linear and the adsorption process was exothermic. The reactivity of E1 under aqueous suspensions of CuSe exposed to visible light exhibited pseudo-first-order kinetics with a rate constant, k, that varied with initial E1 concentration, light power, catalyst dose, and pH. Particularly, k was almost constant over the range pH5–9 but substantially increased as pH rose to 11, while light power and catalyst dose increased k up to a maximum, and the initial concentration reduced k. Surprisingly, CuSe oxidised E1, even in the absence of light, and leached species that were identified and their time-dependency was determined. We concluded that the disappearance of E1 by CuSe is attributed to synergetic effects of adsorption, oxidation by CuSe, and photocatalytic degradation. Supported by liquid-mass spectrometry analysis and molecular chemistry calculations, we also suggested a possible mechanism for E1 degradation. Thus, hexagonal CuSe nanocrystals can be a promising candidate for the treatment of endocrine-disrupting chemicals (EDC)-contaminated wastewaters.

1. Introduction

Since the beginning of global industrialization, endocrine-disrupting chemicals (EDCs) have emerged as severe contaminants in soil and aquatic environments posing potential threat to human health and aquatic biota. These chemicals comprise substances such as steroid hormones, pesticides, plastic additives, and industrial detergents. They can interfere with the normal endocrine system of living organisms, even at very low concentrations (~0.1–10 ng/L) (Pratush et al., 2020; Adeel et al., 2017), and have been linked to several other diseases such as neurological disorders, infertility, and increased incidence of cancers in humans, as well as alteration of reproductive functions of aquatic

lives, leading to almost extinction of some fish species in certain lakes (Adeel et al., 2017; Arguello-Pérez et al., 2019). Amongst EDCs, steroid estrogens have recently gained notable attention, due to their rapidly increasing concentrations in soil and water all over the world and extremely high endocrine disruption potency. This is mainly caused by the increasing tendency of relying on treated wastewater as a means of water supply resource for irrigation and even for potable use especially in the regions experiencing severe water shortage (Lian et al., 2021; Karthik et al., 2022). Both natural (e.g. estrone (E1), 17-β estradiol (E2), estriol (E3)), and synthetic estrogens (e.g. 17α- ethinylestradiol (EE2)) are commonly found in wastewater treatment plant (WWTP) effluents and receiving waters (Lian et al., 2021; Weizel et al., 2021). Their

obvious presence in WWTP effluents and receiving environments is routed to the inadequate removal of estrogens in conventional WWTPs, posing potential threats to exposed aquatic species and humans via intake of affected waters (Amin et al., 2018; Lian et al., 2021; Weizel et al., 2021). In particular, E1 is considered as a crucial EDC due to its high estrogenic activity and persists through biological treatment processes since it is the metabolite and degradation product of other estrogens (Liu et al., 2012). E1 is also commonly detected at much higher concentrations than its counterpart estrogens in wastewater treatment plants (WWTP) (Tang et al., 2020).

Several physical, chemical, and biological treatment methods have been developed in the past few decades for the removal of EDCs but most of them are not sustainable options (Lian et al., 2021). For instance, adsorptive removal, coagulation, and biodegradation methods have been proven to be not stand-alone techniques, hence, less effective for removing estrogens at trace levels, necessitating the use of cutting-edge treatment options (Zhang et al., 2022). Membrane technologies including microfiltration, ultrafiltration, nano-filtration and reverse osmosis are leading candidates for advanced water treatment but membrane fouling remains a major drawback for their extensive use (Fredj et al., 2015).

Photocatalytic degradation of estrones has been considered as one of the most prominent decontaminating procedures in the aquatic environment due to its technological efficacy, sustainability, and environmental friendliness (Perondi et al., 2020). In particular, UV-assisted TiO$_2$-based photocatalysis has mainly served as a template for estrogens decontamination from wastewater mainly due to its chemical stability, low toxicity, and tuneable physicochemical properties (Cai et al., 2021; Gabet et al., 2021). Several researchers have investigated the photocatalytic degradation of estrogens and reported that the estrogenic activity of E2 was lost concurrently with the initiation of its photocatalytic degradation by TiO$_2$ suspension under UV irradiation yielding intermediate products with negligible estrogenic potency (Perondi et al., 2020). They proposed, as further confirmed by other researchers (Cai et al., 2021; Gabet et al., 2021), that E2 completely mineralizes to CO$_2$ after complete degradation. (Puma et al., 2010) reported profound photocatalytic oxidation of a multicomponent mixture of estrogens (E1, E2, EE2, and E3) in the presence of TiO$_2$ suspension under UVC irradiation. However, one of the major drawbacks to TiO$_2$-based photocatalysis is linked to its wide energy bandgap (~3.1–3.5 eV) which limits the utilization of solar spectrum at its maximum (UV accounts for ~4 % of the total natural light spectrum) thus sparking the need to develop a visible-light-active efficient photocatalyst. Despite the above reports, the visible-light induced photocatalytic degradation of E1 is scare (Mukherjee et al., 2017).

Copper selenide is a unique, significantly eye-catching, visible-light-active metal chalcogenide that exists in multiple structural forms such as cubic (Cu$_2$Se), hexagonal (CuSe, Cu$_{0.87}$Se), orthorhombic (CuSe$_2$), and tetragonal (Cu$_3$Se$_2$) (Liu et al., 2017). Due to its exceptional structural features and variable bandgap in the range of 1.4–2.2 eV, it has been extensively investigated for photocatalysis, solar cells, thermoelectric convertors, photo-detectors, and in photo-thermal treatment of cancer cells (Kevorkyants et al., 2022). Recently, Cu$_{2-x}$Se crystals and their nanocomposites have emerged as effective and efficient visible-light-responsive photocatalysts for the degradation of toxic pollutants such as dyes, pharmaceuticals (Iqbal et al., 2021; Murtada et al., 2020), and also for hydrogen production by water splitting (Chakraborty et al., 2020). The state-of-the-art literature search has revealed that no studies have been carried out on E1 removal by CuSe photocatalyst.

Furthermore, E1 is known to be a primary degradation by-product of other steroidal estrogens making it widely available in a variety of aquatic environments (Zhang et al., 2022). Nonetheless, correlating the fundamental stages involved in photocatalytic degradation with the removal kinetics data is crucial for a comprehensive understanding and optimization of the process variables involved in E1 decontamination. Another aspect of E1 photocatalytic degradation that has not received enough attention is the need to understand the degradation pathways of E1 and pertinent role of the photocatalyst in order to comprehend its degradation mechanism.

Therefore, the key literature gaps to be considered in this work were (i) visible-light-induced photocatalytic degradation of E1 (ii) the variables affecting E1 photocatalytic degradation effectiveness, and (iii) peculiar role of CuSe toward the degradation mechanism of E1. In this context, we synthesized visible-light-responsive CuSe hexagonal nanocrystals through a facile, scalable low-temperature co-precipitation method, and evaluated its contribution to the degradation of estrone (E1) for the first time. Nanoflakes of CuSe presented synergetic effects of adsorption, oxidation, and photocatalytic degradation for E1 elimination due to their considerably low band gap and enhanced surface area. Detailed degradation mechanism was also suggested on the basis of liquid mass spectrometry analysis and molecular chemistry calculations. Finally, our work shows an effective avenue for a broad range of EDC removal from wastewater under visible-light illumination.

2. Experimental

2.1. Synthesis of CuSe nanoflakes

All reagents were of analytical grade. An aqueous solution of CuSO$_4$0.5H$_2$O (1 mmol, 0.249 g) was added to a moderately brown coloured solution of powdered Se (1 mmol, 0.079 g) in hydrazine hydrate. Stirring of the reaction mixture for 30 min at 20 ^{o}C led to gradual change of the solution colour, from moderate brown to darkest brown. Further stirring of this reaction mixture at 100 ^{o}C for 50 min resulted into black coloured precipitates of CuSe nanocrystals. After cooling down to room temperature, the precipitates were collected by centrifugation at 5000 rpm for 20 min followed by washing with deionised water and ethanol several times. The washed precipitates were dried in vacuum oven (Thermo- Scientific, 3625 A) for 8 h at 60 ^{o}C and were stored in a desiccator for further analyses. A schematic layout of CuSe synthesis is illustrated in Supplementary Information Fig. S1(a).

2.2. Photodegradation of E1

Catalyst powder (0.5 g/L) was dispersed in 100 mL aqueous solution of 1 mg/L E1 (details of E1 solution preparation are provided in the Supplementary Information S1). The dispersion was stirred using magnetic stirrer with a polytetrafluoroethylene (PTFE)-coated magnetic stir bar for about 30 min in dark to obtain complete adsorption-desorption equilibrium. The equilibrated solution was then irradiated through a fibre optic light guide (5 mm diameter) fitted to light source (JENA LQ-HXP 120UV/150.26 C; λ = 300–700 nm). The tip of fibre optic was placed vertically above the solution mixture at a distance of 7 cm in laboratory-designed photocatalytic reactor (Supplementary Information S2). Aliquots of E1 solution were collected at regular intervals of time using sampling syringe (BD, Fisher Scientific) and then centrifuged at 13,000 rpm for 5 min (Eppendorf, 5702) followed by filtering out using 13 mm PTFE filter (0.45 μm pore size) to completely remove the catalyst from solution before analysis. We chose this filter because it had the lowest E1 retention as compared to other types of filters (further details can be found in Supplementary Information S3).

The concentration of E1 was determined by HPLC (Agilent 1200 series) equipped with an electrospray quadrupole mass spectrometer (Agilent 6410 series triple quad). The mass spectrometer was operated in a selected-ion-mode (SIM) with negative ionization. The SIM ion (*m/z*) [M-H] for E1 was 269 and the fragmentor voltage was 160 V; preliminary optimised for highest signal. The mobile phase was 50 % methanol (v/v): 50 % aqueous ammonium hydroxide (40 mM); flow rate 0.4 mL/min; and injection volume 10 μL.

2.3. Material characterization

Powder XRD pattern was obtained from Bruker D8 Discover X-ray diffractometer using monochromatic Cu K$_\alpha$ radiations at 40 kV and 40 mA. We used DIFFRAC.EVA V4.3 software for diffraction peak intensities collection, peak indexing, unit-cell parameters refinement, peak integration, background determination, and peak matching. Particle size distribution in aqueous solution was performed on 3000E MAL1123 mastersizer (Malvern Instruments) employing dynamic light scattering (DLS). The Brunauer-Emmett-Teller (BET) surface area was measured at 77 K using N$_2$ (nitrogen) adsorption/desorption isotherms on Nova 200e (Quantachrome Instruments, USA) surface area and pore size analyser. Quantachrome TM NovaWin package was used for data acquisition and analysis. Catalyst sample was analysed for S$_{BET}$, calculated in the range 0.05–0.30 P/Po after degassing at 125 °C for 12 h before nitrogen adsorption measurements. Elemental analysis was obtained using JSM-6510LA SEM (JEOL) microscope coupled with EDX (Oxford instruments) microscope. The morphology and microstructure of the catalyst were characterized by high-angle annular dark-field (HAADF), bright field (BF), and high-resolution transmission electron microscopy (HRTEM) images obtained by Thermo Fisher Talos STEM equipped with HAADF detector operating with an inner angle of 55 mrad at 200 kV. The incident electron beam convergence angle was 21 mrad. The elemental distributions of sample were characterized by energy-dispersive X-ray spectroscopy (STEM–EDX) in the STEM (scanning transmission electron microscope). TEM samples were prepared by dispersing the powder sample in deionized water, sonicating for several minutes, and drop-casting onto a gold grid coated with an amorphous carbon film. X-ray photoelectron spectroscopy (XPS) measurements were obtained via Axis Supra XPS (Kratos Analytical) system equipped with monochromatic Al-Kα X-ray source (1486.7 eV) and large area slot mode detector (ca. 300 μm × 800 μm analysis areas). Charge neutralization was done to limit differential charging for each sample, and the data was calibrated for the C 1 s peak (284.8 eV). Spectra were recorded with the following settings: dwell time 0.1 s, step size 1 eV, pass energy 160 eV (survey spectra) and dwell time 250 ms, step size 0.1 eV, pass energy 20 eV (high-resolution spectra). The recorded data were analysed using CASA XPS software (Version 2.3.12.8). UV-Vis measurements of CuSe were taken from Lambda 365 UV/Vis spectrophotometer (Perkin Elmer). We ultrasonically dispersed 0.001 g/mL of powdered catalyst in 20 % dilute ethanol solution for optical absorption measurements.

2.4. Reaction by-products

Determination of the by-products was made using direct-injection-electrospray ionisation (ESI) LC/MS/MS analysis in negative mode. The mass spectra were collected with a scan range *m/z* 50–500. The mass spectrometry analysis was supported by computational chemistry calculation using Gaussian 16 W with Gaussian view 6.1 for all the quantum chemical calculations. The geometries of studied molecules were optimised using hybrid Density Functional Theory (DFT), B3LYP, with the 6–31 G(d,p) basis set. Active sites were determined by Fukui functions calculated based on Mulliken atom charges determined by Gaussian analysis (Liu et al., 2014a; Lu and Chen, 2012). The Fukui functions (*f*) are widely applied to examine the electrophilic, nucleophilic, and radical reactions (Dwinandha et al., 2022; Rokhina and Suri, 2012). According to Fukui's theory, the electron rich areas of the molecule are more susceptible to electrophilic attack, whereas the electron poor areas are more prone to nucleophilic attack. In this study, the radical susceptibility of E1 was determined according to the radical Fukui function index, f^0, estimated by Eq.1. The large value of f^0 at a particular site of the molecule implies high reactivity of that site with the radical.

$$f^0 = \frac{q(N+1) - q(N-1)}{2} \tag{1}$$

where *q* denotes the Mulliken charge and *N* the number of electrons in the molecule. The Mulliken charge was calculated by Gaussian.

3. Results and discussion

3.1. Catalyst characterization

3.1.1. Structural analyses

Powder XRD pattern of CuSe nanocrystals (Fig. 1a) illustrates characteristic peak pattern of CuSe (COD-9000063, space group *P63/mmc*). Diffraction peaks positioned at 26.03°, 26.54°, 28.01°, 31.11°, 41.03°, 45.29°, 46.02°, 49.98°, 53.83°, 54.76°, and 56.54° are indexed to (100), (101), (102), (103), (006), (008), (107), (210), (108), (201), and (216), respectively. In addition, the diffraction pattern shows a strong (006) diffraction peak as compared to the standard pattern (102) indicating that the synthesized catalyst has crystalline orientation towards <001> direction (Liu et al., 2014b). These results also indicate that the synthesized material has perfectly crystallized into a single-phase, stoichiometric CuSe with lattice constants *a* (=*b*) = 3.94 Å and *c* = 17.25 Å, which is in corroboration with previous studies (Liu et al., 2014b). Fig. 1b illustrates EDX elemental mapping and chemical composition (inset) of the synthesized sample revealing the phase-pure formation of copper selenide having Cu/Se ratio close to 1:1, as predicted by XRD and is equivalent to the ratio of Cu:Se used in the preparation of the catalyst.

We further verified the elemental composition and chemical states of the constituent elements by performing XPS analysis. The elemental survey spectrum, as illustrated in Fig. S2, indicates the presence of copper and selenium elements confirming phase purity of the synthesized material. The presence of trace amounts of oxygen could be attributed to adsorbed atmospheric oxygen. The high-resolution core-level spectra of Cu (2p) (Fig. 1c) show a distinctive doublet with Cu 2p$_{3/2}$ at 932.2 eV and Cu 2p$_{1/2}$ at 951.2 eV suggesting Cu (I) or Cu (0). These binding energies nicely matched with the previously reported values in the literature (Wang et al., 2014; Xu et al., 2015; Yang and Hsiang, 2018b). The satellites usually associated with Cu (II) are minimal, although peak deconvolution suggested some Cu (II) is present, with a side peak in the Cu 2p$_{3/2}$ present at 933.9 and 954.3 eV in Cu 2p$_{1/2}$, which is close to the reported values (Liu et al., 2011; Riha et al., 2011). Nonetheless, Cu 2p (I) and Cu 2p (II) were found to be 60.2 % and 39.8 %, respectively in the synthesized sample. These observations confirmed the presence of Cu in + 1/+ 2 mixed oxidation states in all the compositions which might be attributed to surface oxidation. However, the associated Cu Auger kinetic energy of 917.4 eV suggests the surface Cu is predominantly Cu (I) (Xu et al., 2015; Zhang et al., 2011). Fig. 1d reveals the Se (3d) spectra of synthesized sample showing strong primary peaks at 54.8 and 55.7 eV for Se 3d$_{5/2}$ and Se 3d$_{3/2}$, respectively,(Yang and Hsiang, 2018a; Zhang et al., 2010) with a small side peak at 59.4 eV that is attributed to some surface SeO$_x$ (Naumkin et al., 2012). The sample surface was partly oxidized, as indicated by the presence of oxygen (Fig. S2) due to the readily oxidizing nature of copper-containing compounds (Singh et al., 2018); besides, the sample synthesis and processing has been taken place in air. XPS measurement reveals the oxidation states of Se and Cu in the synthesized sample as −2, + 1, or + 2, respectively.

3.1.2. Morphology, microstructure, and surface area

The morphological investigations of synthesized catalyst are presented in Fig. 2a–f. The SEM images of as-synthesized catalyst sample (Fig. 2a–c) reveal a hexagonal, flake-like surface morphology with an average particle size of about 0.229 ± 0.146 μm and thickness of 0.05
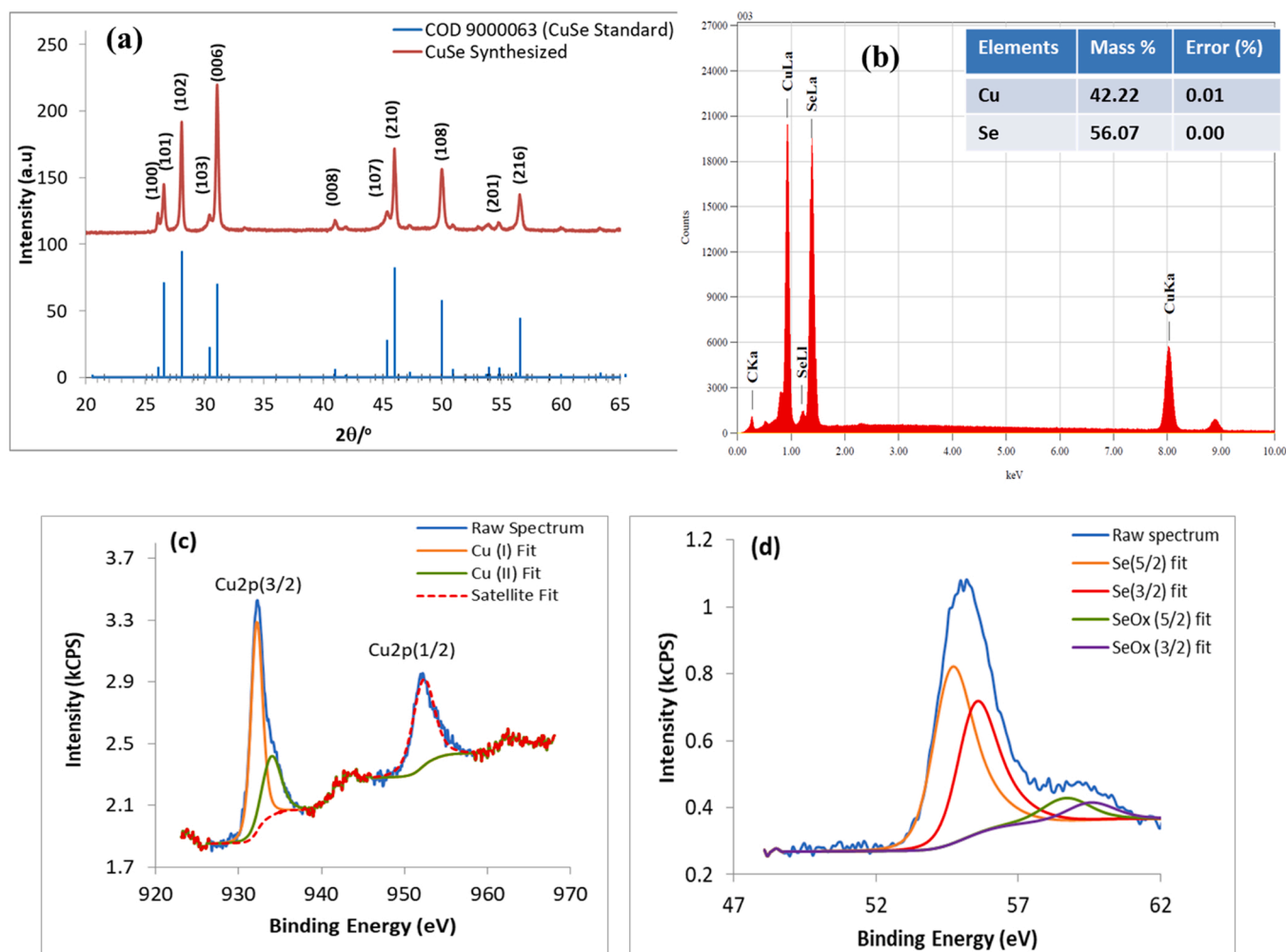
Fig. 1. Structural analyses of CuSe nanoflakes **(a)** Powder X-Ray diffractogram, **(b)** elemental mapping (EDX), **(c-d)** High resolution XPS Cu 2p and Se 3d region spectra of $Cu_{2-x}Se$ prepared at different reaction temperatures. Panel **(c)** corresponds to Cu 2p spectra containing the raw spectrum and peak fits for Cu 2p species ($Cu2p_{3/2}$, $Cu2p_{1/2}$ for both Cu^+ and Cu^{2+}) and satellite peaks of Cu^{2+}. Panel **(d)** corresponds to Se 3d containing the raw spectrum, peak fits for Se species (Se $3d_{3/2}$, Se $3d_{5/2}$) and intermediate selenium oxides.

± 0.02 μm. Fig. 2d demonstrates a wide range of particle size distribution ranging from nanometre to micrometre with the most abundant sizes are in the range 100–200 nm. TEM images (Fig. 2e-f) demonstrated laminar morphology and preferred hexagonal shape of CuSe flakes. The crystals aggregated together when drop-cast on the TEM grids, thus their size distributions were difficult to acquire, but the size generally falls in the range of tens of nanometers to several micrometres for the synthesized sample. The obtained HRTEM images in Fig. 2e confirm that the CuSe crystals have a hexagonal closed packed (*hcp*) structure that can be indexed by the hexagonal CuSe structure (*P63/mmc*) (Criddle and Stanley, 2012). The interplanar spacing of crystal planes marked by pairs of yellow lines were measured to be in the range 3.30–3.40 Å, which correspond to the ($10\bar{1}0$) planes of bulk CuSe (Peiris et al., 1998; Criddle and Stanley, 2012). The elemental distributions of Cu and Se from the EDX signal mapping results (Fig. 2f) demonstrate that both Cu and Se dispersed homogeneously in the crystals, which further confirms the formation of single-phase copper selenide nanostructures.

Particle size distribution analysis from dynamic light scattering performed on the samples dispersed in aqueous solutions yielded a wide particle size distribution with 90 % of particles have sizes < 802 nm while the average particle size was 171 ± 0.2 nm, which corroborates with the SEM findings. The BET analysis revealed that synthesised catalyst had a BET surface area of 11.0 m^2/g and was a non-porous material since both the external surface area and the measured BET area were equivalent (Supplementary Information S4).

3.1.3. Optical properties

To analyse the optical properties of as-synthesized copper selenide, we obtained room temperature UV-Vis absorption spectra, as shown in Fig. 3. It is evident from Fig. 3 that a broad absorption peak appears in the wavelength range of 400–700 nm for the catalyst. The band gap value of the catalyst was calculated by fitting Tauc's relation (Eq.2). (Mukherjee et al., 2017)

$$\alpha h\upsilon = A(h\upsilon - E_g)^n \tag{2}$$

Where α is absorption coefficient, A is constant, E_g is bandgap, $h\upsilon$ is the photon energy and n is the exponent which determines the type of the electronic transition causing absorption, $n = 1/2$ for direct band-band transition.

The inset of Fig. 3 depicts a calculated bandgap value of 1.60 ± 0.01 eV for CuSe, suggesting visible-light responsive nature of the photocatalyst. This bandgap value nicely matches with the previously reported values for CuSe nanomaterials in the literature(Liu et al., 2017, 2015). It is known that bulk CuSe possesses narrow band-gap energies with both indirect and direct bandgap energies in the range of 2.1–2.3 and 1.0–1.4 eV, respectively (Liu et al., 2015; Wang et al., 2016). The slight decrease in direct bandgap of the as-synthesized CuSe catalyst
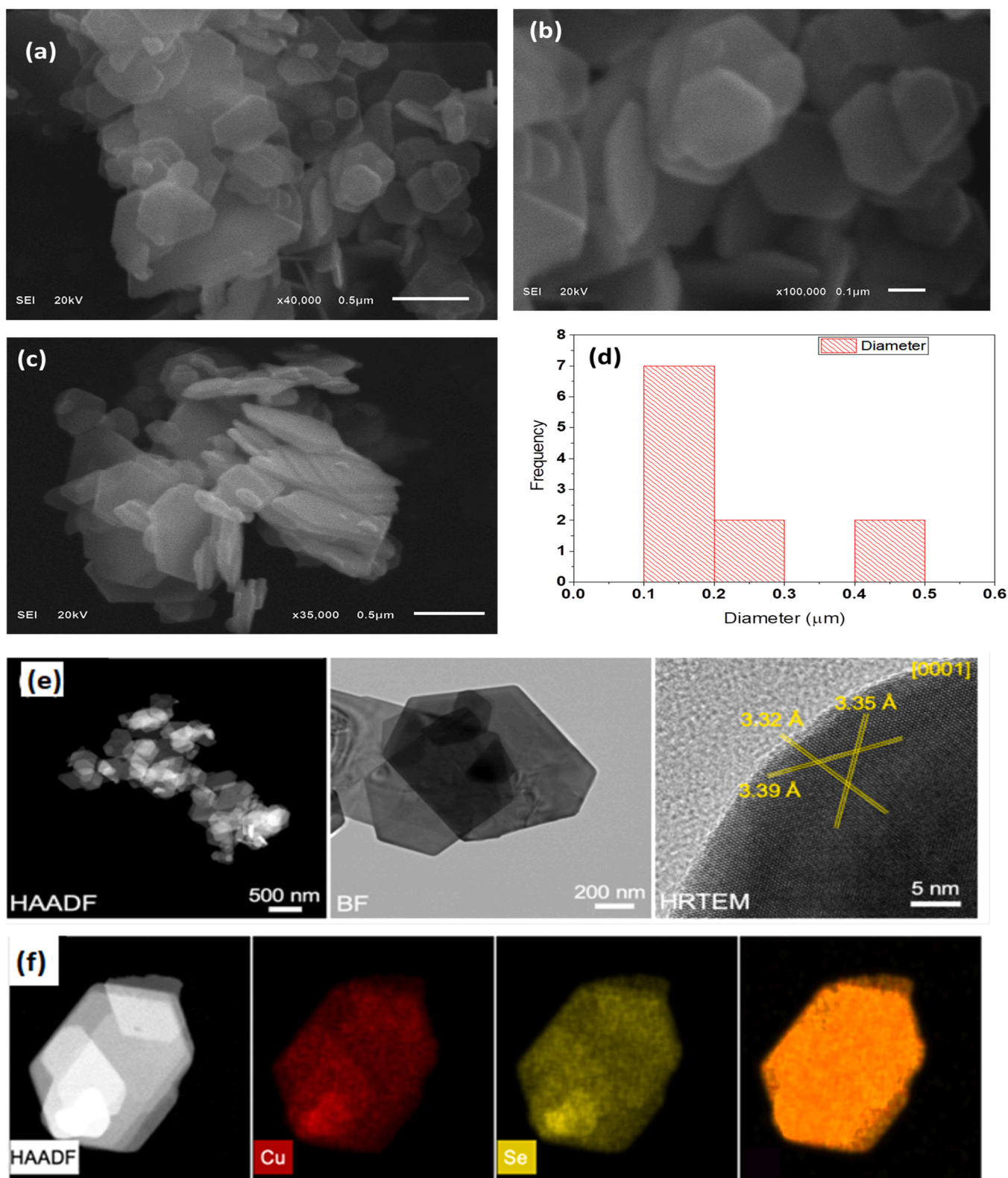
Fig. 2. **(a)** Low-magnification **(b)** high-magnification **(c)** lateral view SEM images of CuSe hexagonal flakes **(d)** Particle size distribution histogram **(e)** Typical HAADF, BF and HRTEM images of the CuSe. The inserted values show the interplanar spacing of the crystal planes that are marked by pairs of yellow lines. **(f)** Typical HAADF image and corresponding elemental distributions of Cu (red), Se (yellow) and hybrid, for CuSe.

indicates red-shift which is most likely due to surface effects and defects formation (Shi et al., 2013). Similar observations have also been reported by (Liu et al., 2017).

3.2. Adsorption of E1 on hexagonal CuSe nanoflakes

The adsorption capability of the synthesized catalyst was evaluated by investigating the thermodynamics and extent of E1 adsorption. We
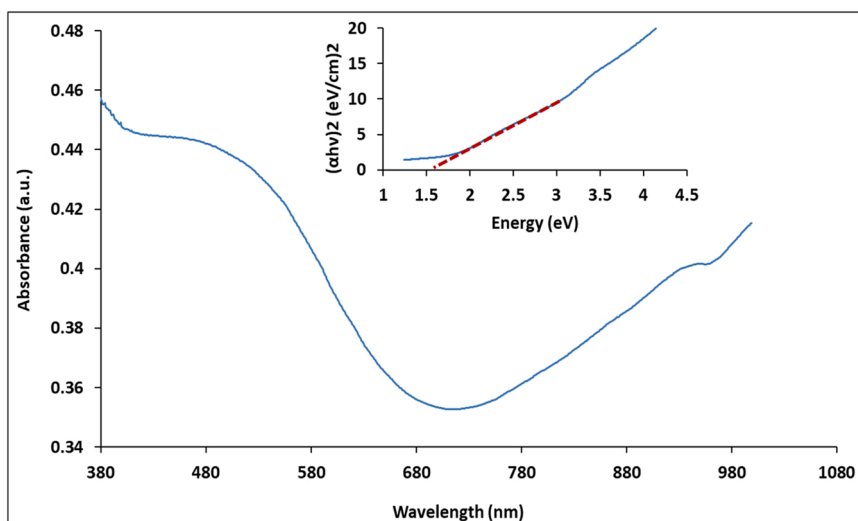
Fig. 3. Room temperature UV–Vis absorption spectrum of CuSe nanoflakes dispersed in dilute ethanol; Inset: Tauc plot for CuSe nanocrystals.

performed a series of adsorption experiments at different temperatures and adsorbent dosages. The results showed a linear relationship between the equilibrium adsorption uptake (q_e) and the solution concentration (C_e) at all the working temperatures (15–35 °C) as described by Eq. 3 (Honorio et al., 2018). This linear equilibrium relationship is a plausible result, due to dilute concentrations (initial solution concentration 1 mg/L) used in this study and is in line with previously published data (Ben Fredj et al., 2015). The K-values were then correlated to solution temperatures using Van't Hoff equation (Eq. 4) and free Gibbs energy is given by Eq. 5 (Honorio et al., 2018).

$$q_e = KC_e \tag{3}$$

$$Ln(K) = \frac{\Delta S}{R} - \frac{\Delta H}{RT} \tag{4}$$

$$\Delta G = -RTLn(K) = \Delta H - T\Delta S \tag{5}$$

Where, C_e and q_e are equilibrium concentration of E1 in solution and adsorption uptake of E1 at equilibrium, respectively; K is equilibrium constant of adsorption; ΔS, ΔH, and ΔG are the adsorption entropy, enthalpy, and Gibbs free energy respectively; R is the ideal gas constant (R=8.314 J/K/mol); and T is the absolute temperature (K).

We obtained the thermodynamic parameters (i.e., ΔS, ΔH, and ΔG) by plotting the natural logarithm of adsorption constant K against the inverse of the working temperatures (Eq. 4). As can be seen in Fig. S3 (Supplementary Information), a good fit of the experimental data with the model was obtained (R^2 =0.968). According to Table S2 (Supplementary Information), negative values of ΔH and ΔS demonstrate the exothermic nature of adsorption and decreased randomness at the adsorbent surface upon uptake of E1 from aqueous solution, respectively. The spontaneity of adsorption is supported by negative values of ΔG, while these values become more negative at low temperature suggesting the feasibility of adsorption at lower temperatures, which is in line with the fundamental theories of adsorption. Moreover, the magnitude of the heat of adsorption ($|\Delta H| < 63$ kJ/mol) indicates that the adsorption of E1 on CuSe nanocrystals tends to be between physisorption and chemisorption processes (Wilcox, 2012). The obtained thermodynamic values are comparable to those reported by other researchers for the adsorption of estrone (Honorio et al., 2018).

We have also evaluated the kinetics of E1 adsorption onto CuSe and found that the adsorption rate was initially rapid until about 30 min, whereafter, it gradually evolved to reach a plateau at about 90 min (Fig. 4). To further examine the adsorption kinetics of E1 onto CuSe, the widely used pseudo-first-order (PFO) and pseudo-second-order (PSO)
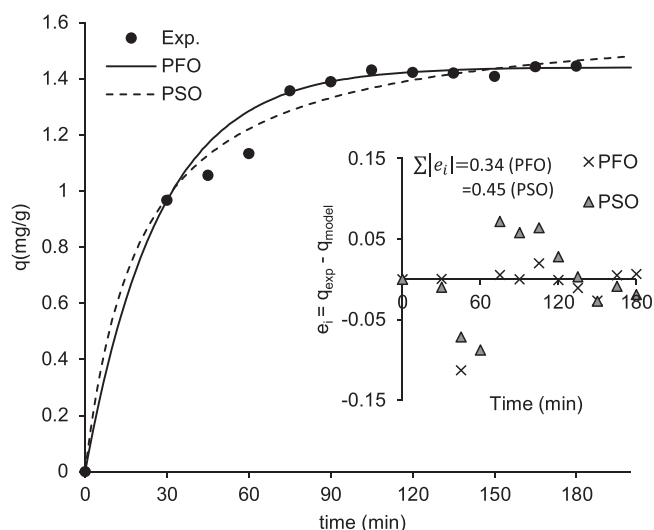

Fig. 4. Adsorption of E1 on CuSe (Initial E1 conc. C_0 =1 mg/L; catalyst dose=0.5 g/L; neutral pH and 20 °C).

adsorption kinetic models, which are shown by Eqs. 6 and 7 (Honorio et al., 2018), respectively, were employed to model the experimental data and determine the model parameters by fitting.

$$q = q_e(1 - \exp(-k_1 t)) \tag{6}$$

$$q = \frac{q_e^2 k_2 t}{1 + q_e k_2 t} \tag{7}$$

Where q and q_e are the adsorbent uptake concentrations in *mg/g* at time t and at equilibrium, respectively (*mg/g*); k_1 and k_2 are the PFO and PSO adsorption rate constants in *min^{-1}* and *g/(mg.min)* respectively.

PFO was found a suitable model to fit the data better than PSO as demonstrated by a lower sum of the absolute values of the residual errors, e_i, (Fig. 4). The values of parameters k_1 and q_e for PFO were 0.037 min^{-1} and 1.44 mg/g, respectively and the values of k_2 and q_e for PSO were 0.031 g/(mg.min) and 1.63 mg/g, respectively. The value of k_1 obtained in this study is about three times higher than that obtained by (Elias et al., 2021) for the adsorption of E1 onto nutshell activated carbon and is about 12 times higher than E1 adsorption on electrospun nanofibers reported by (Yasir et al., 2021) but is less, by about 5times,

than that reported for multi-walled carbon nanotubes (Prokić et al., 2022).

3.3. Photocatalytic activity under visible-light irradiation

Using CuSe nanoflakes as photocatalyst, we performed photocatalytic degradation studies on E1 solution under visible-light irradiation. The samples were stirred for about 30 min in dark followed by exposure to light for 180 min. In addition, we evaluated in control experiments, the photolysis of E1 (i.e., degradation of E1 without catalyst) and the adsorption of E1 on the catalyst in dark, as shown in Fig. 5a. It was noticed that E1 did not degrade under the Hg-Xe lamp irradiation (120 W) in the absence of catalyst (Fig. 5a), which is in agreement with the reported literature which showed negligible extent of E1 photolysis under UVA-visible light (Han et al., 2012). Fig. 5a also reveals that the catalyst adsorbs E1 in dark followed by saturation in ~90 min while significantly degrades E1 to ~90 % under visible-light irradiation. The extent of degradation gradually saturates however, does not reach the complete degradation till 180 min

The reaction kinetics of photocatalytic degradation of E1 can be obtained using the Langmuir-Hinshelwood model. At low concentrations, the model can simply be described by a pseudo-first order-reaction kinetics leading to Eq. 8 (Reddy et al., 2020) after integration.

$$Ln\left(\frac{C_0}{C_t}\right) = kt \tag{8}$$

Where, C_0 and C_t are solution concentrations at times $t = 0$ and t, respectively, and k is the degradation rate constant (min^{-1}) which was determined by linearly fitting the quantity $ln(C_0/C_t)$ versus time t; its value was found to be 0.013 min^{-1} and R^2 was 0.9905.
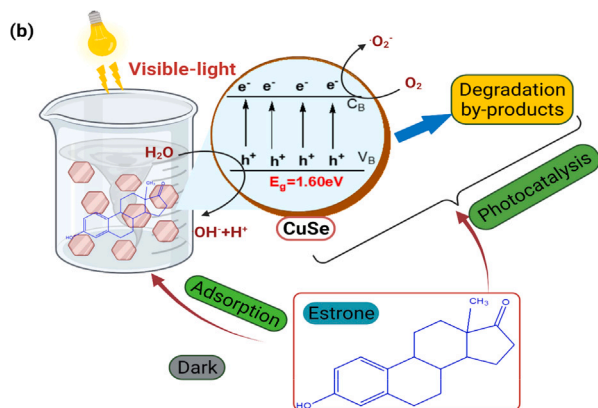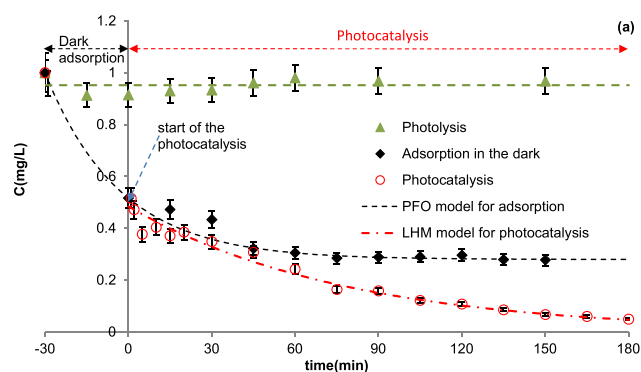

Fig. 5. (a) Photolysis, adsorption, and CuSe photocatalytic degradation of E1 (Initial E1 conc. $C_0 = 1$ mg/L; catalyst dose = 0.5 g/L; neutral pH and 20 ^{o}C) **(b)** Schematic-layout of processes taking place at the interface of CuSe nanoflakes and E1 in the solution in the absence/presence of light irradiation.

To obtain insight into the photodegradation process, Fig. 5b illustrates the schematic layout of the reaction mechanism. Generally, for undergoing photo-induced reactions, the hexagonal CuSe must absorb incident visible-light energy comparable to its bandgap (1.60 eV) resulting in the excitation of valence band (V$_B$) electrons (e-) to the conduction band (C$_B$) whereby leaving behind positively-charged holes (h^+) in the V$_B$, as illustrated in Fig. 5b. These photo-generated electron/hole pairs oxidise the adsorbed species such as water on the surface of copper selenide nanocrystals producing hydroxyl radical ($^•$OH) and oxygen radical ($O_2^{-•}$). These reactive oxygen species not only react with each other but most importantly participate in the degradation of estrone (E1) into intermediates, as shown by following reactions (Eqs. 9–16), which is in-line with previously reported literature (Ali et al., 2018; Chen et al., 2019; Liu et al., 2017; Mkhalid, 2016). Indeed, the mechanism of photocatalytic degradation of organic molecules in water involves several adsorption-reaction-desorption steps (Turchi and Ollis, 1990; Srinivas et al., 2019). The adsorption and desorption steps are governed by diffusion processes while the oxidation reactions are initiated by oxygen and water adsorbed on the photocatalyst through interactions with the positive holes of the valence band h^+ to generate hydroxyl radicals that react with the organic molecules either in the bulk solution or on the surface of the catalyst (Eqs. 9–16).
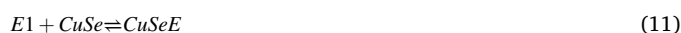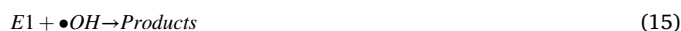
Light absorption:

$$CuSe \xrightarrow{visible light} CuSe(h_{VB}^+ + e_{CB}^-) \tag{9}$$

Charge carrier recombination:

$$h_{VB}^+ + e_{CB}^- \rightarrow heat \tag{10}$$

Adsorption step:

$$E1 + CuSe \rightleftharpoons CuSeE \tag{11}$$

Charge-carrier trapping:

$$CuSe(h_{VB}^+) + H_2O \rightarrow H^+ + \bullet OH \tag{12}$$

$$CuSe(e_{CB}^-) + O_2 \rightarrow O_2^{-\bullet} \tag{13}$$

$$CuSeE1 + h_{VB}^+ \rightleftharpoons CuSeE1^+ \tag{14}$$

Hydroxyl radical reactions:

$$E1 + \bullet OH \rightarrow Products \tag{15}$$

$$CuSeE1 + \bullet OH \rightarrow Products \tag{16}$$

The significant photodegradation of E1 by CuSe nanocrystals can be attributed to enhanced light absorption capability and increased separation of e-h pairs in this catalyst, as reported by other researchers (Gao et al., 2016; Ghosh et al., 2016; Liu et al., 2017). These findings reveal that the presence of a CuSe catalyst can effectively cause the photocatalytic degradation of E1, confirming the role of CuSe in the photodegradation of E1.

3.3.1. Dependent factors of photodegradation performance of the catalyst

For understanding the detailed catalytic performance of E1 photodegradation, the influence of various experimental variables including catalyst dose, initial E1 concentration, solution pH, light intensity, and solution temperature on the extent of photodegradation was investigated, as shown in Fig. 6(a-e). We tested the photocatalytic degradation of E1 at initial concentrations (C_0) in the range of 0.5–2.0 mg/L while keeping the catalyst dose constant at 0.5 g/L (neutral pH and 20 ^{o}C). An inverse relationship was noticed between the extent of photodegradation and initial E1 concentration (C_0) as illustrated in Fig. 6a. These findings perfectly corroborate the reported literature on photocatalytic degradation of estrone (Han et al., 2012). Indeed, for a four-fold increase in concentration from 0.5 to 2 mg/L, the photocatalytic rate constant was reduced by nearly half from 5.3×10^{-3} to
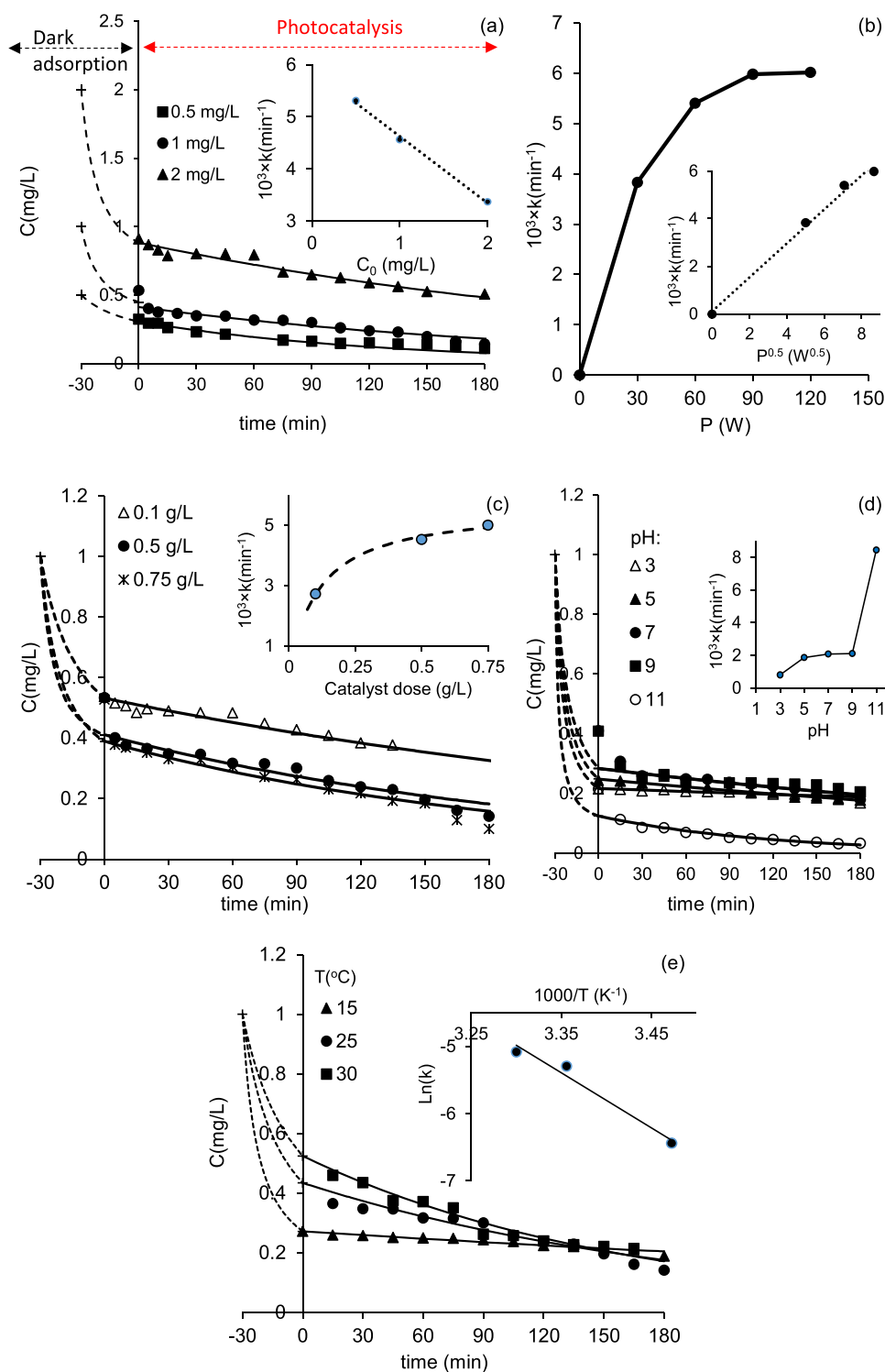
Fig. 6. (a) Effect of initial E1 conc. (C_0) (catalyst dose=0.5 g/L; neutral pH, irradiation power=60 W, and 20 °C); **(b)** effect of irradiation power (C_0=1 mg/L, catalyst dose=0.5 g/L; neutral pH, and 20 °C); **(c)** Effect of catalyst dose (C_0=1 mg/L, neutral pH, irradiation power =60 W, and 20 °C); **(d)** effect of pH (C_0 =1 mg/L, catalyst dosage=0.5 g/L; irradiation power =60 W, and 20 °C); **(e)** effect of temperature (C_0 =1 mg/L, catalyst dosage=0.5 g/L; irradiation power=60 W, and neutral pH).

3.3×10^{-3} min^{-1} (Fig. 6a inset). This reduction in the rate of degradation might be explained by the increased number of molecules to degrade as the initial concentration of E1 increased whilst the generation rate of reactive species (e.g., •OH) remained constant since the intensity of light remained constant. In addition, as the initial concentration increases, the surface of catalyst becomes more saturated, which could also reduce the generation of the oxidative species by blocking a portion of the catalyst surface area being accessible to photons (Han et al., 2012). Therefore, by increasing the initial concentration of estrone, the rate of photocatalytic degradation decreases.

The influence of irradiated intensity on the photodegradation of E1 was determined by performing experiments at different light intensities adjusted to power values of 30, 60, 90, and 120 W by the dimming knob of the light source; the other conditions were C_0 (E1) of 1 mg/L, catalyst dose of 0.5 g/L, and neutral pH. Fig. 6b clearly shows that the rate of photocatalytic degradation increases with increasing the irradiation light intensity, which is obviously due to the availability of a greater flux of photons as the light intensity increases. However, such an increase of the photocatalytic reaction rate constant, k, is limited to a saturation value at high light intensity (120 W) indicating that the reaction is

completely limited by its intrinsic kinetics. At high light intensity, all the active sites of the photocatalyst are permanently active due to the high photon flux and the catalyst behaves like an ordinary heterogeneous catalyst (Bloh, 2019). However, below the saturation light power (P < 90 W), the reaction rate constant presents half-order dependency with light intensity (Fig. 6b inset), which is in good agreement with the literature (Mills et al., 2015). According to these results, an irradiation power of 60 W was selected for further photodegradation studies.

The effect of catalyst dose on the extent of degradation was determined, as illustrated in Fig. 6c, by testing different catalyst dosages 0.1, 0.5, and 0.75 g/L using irradiation power of 60 W, and C_0 (E1) of 1 mg/L. Fig. 6c shows a characteristic pattern of the variation of extent of degradation with catalyst dose, i.e., photodegradation increases with increasing the catalyst dose. At the lowest catalyst dose (0.1 g/L), E1 barely degrades up to 60 % after 180 min, while it degrades more than 82 % by increasing the catalyst dose to 0.50 and 0.75 g/L within the same time. A further increase in catalyst dose to 1.0 g/L (figure not shown here) resulted in a decrease of E1 degradation, which could be due to a reduced light transmission in the solution that was noted by visual observation as well that the solution became a thick slurry at the catalyst dose of 1.0 g/L. The effect of catalyst dose on the photocatalytic rate constant is shown in Fig. 6c inset. As the catalyst dose increased, the rate constant reached a saturated value at about 0.75 g/L, which is in agreement with a fundamental photocatalytic kinetics study reported by Bloh (2019). The direct dependence of the extent of E1 photodegradation on catalyst dose could be attributed to the fact that an appreciable amount of photocatalyst in the solution provides enhanced contact sites between the catalyst and E1(Han et al., 2012). However, increasing the catalyst dose beyond a certain optimum dose results in the light penetration becoming too weak, which will limit the efficiency of the photocatalytic process (Kumar and Pandey, 2017). In this study, we found that a catalyst dose of 0.5 g/L was a plausible dose to carry out further evaluations of the photocatalytic degradation of E1.

The solution pH is a crucial parameter that affects the photocatalytic degradation of a pollutant in the aquatic environment (Mukherjee et al., 2017). The experiments were conducted at different pH values of 3, 5, 7, 9 and 11 using an irradiation power of 60 W, C_0 (E1) of 1 mg/L and catalyst dose of 0.5 g/L. The results presented in Fig. 6d show that maximum photodegradation (98 %) occurs at pH 11, while a marginal increase in degradation was observed as pH raised from 3 to 9 (~80 %). The effect of pH is observed when we plotted the photocatalytic rate constant versus pH (Fig. 6d inset), which shows a slight increase in the rate with increasing pH up to 9 followed by a sharp rise at pH 11. These results are similar to those reported by (Coleman et al., 2000) for E2. This trend of pH effect could be attributed to enhanced photodegradation of E1 at alkaline pH since the molar absorption coefficient of E1 at alkaline pH (9.26×10^3 cm^{-1}M^{-1} at 298 nm) is about five times higher than that at acidic pH (1.85×10^3 cm^{-1}M^{-1}) (Hurwitz and Liu, 1977). Moreover, as the pH increases, the hydroxyl ion concentration at the active sites increases thereby increasing the production of hydroxyl radicals. However, the point of zero-charge (pzc) of the catalyst was found at pH 6.4 (Supplementary Information Fig. S4), which implies that the surface of CuSe is deprotonated to a negative charge at pHs higher than pzc. Thus, the increase in pH up to 9 favours the repulsion of hydroxide ions while giving less competition for the active sites to attract E1, which has a neutral charge because its pKa is ≈ 10.4 (Hurwitz and Liu, 1977). This compromise between two competing mechanisms could explain the plateaued value of the rate constant as pH increased to 9. A further increase in pH to 11 results in significant deprotonation of E1 (~80 % of E1 is deprotonated; Supplementary Information Fig. S5). As E1 deprotonates and becomes negatively charged, its repulsion with the catalyst becomes significant implying that hydroxide ions become more favourably attracted to the surface of the catalyst, given their high concentration (1 mM) compared to E1 (<0.003 mM). This would then result in high concentrations of hydroxyl radicals attacking E1. In addition, the deprotonation of the OH group in E1 would also increase

the reaction rate with free radical species (O'shea and Cardona, 1995; Schaefer et al., 2020; Vo et al., 2021).

The temperature dependence on photocatalytic degradation of E1 was investigated by performing experiments at different temperatures in the range 15–30 °C using irradiation power of 60 W, C_0 (E1) of 1 mg/L and catalyst dose of 0.5 g/L. It is evident from Fig. 6e that during the adsorption in the dark (i.e. −30 min≤t ≤ 0), the extent of E1 removal increased as the temperature reduced, which agrees with the discussion presented on the effect of temperature on the adsorption isotherm. However, during the photocatalytic degradation phase (i.e., $0 \leq t \leq 180$ min), an increase in temperature increased the degradation rate of E1. The pseudo-first order-reaction rate constant, k, was determined at different temperatures used and its change with temperature was described using the Arrhenius equation; $k = k_0 exp\ (-E_A/RT)$ (Bloh, 2019). A plot of *Ln (k)* vs the inverse of temperature (*1/T*) is shown in Fig. 6e. The pre-exponential factor, k_0, and the activation energy E_A were determined from the slope and intercept of the line Ln(k) vs 1/T and their values are 4.03×10^9 min^{-1} and 68 kJ/mol, respectively. This value of E_A is about three times higher than typical activation energies reported for other photocatalytic reactions (Acedo-Mendoza et al., 2020; Bloh, 2019; Qin et al., 2020), which implies that the temperature effect is more prominent with CuSe. Therefore, this study shows that the photocatalytic degradation of E1 by CuSe is a temperature-dependent reaction implying that increasing the reaction temperature increases the rate of the reaction (Bloh, 2019).

3.3.2. By-products of estrone photocatalytic degradation reaction and possible mechanism

To aid the understanding of the photocatalytic degradation mechanism of estrone using CuSe, we conducted liquid mass spectrometry analysis (ESI-negative) of samples collected at different reaction times using scans in the range 50–500 mass/charge ratios (*m/z*). Although by-product formation was expected during light exposure, it was remarkable that during adsorption in the dark, new *m/z* signals, apart from *m/z* 269 for E1, appeared and evolved. This indicates that chemical reactions take place even in the dark and the results are discussed next.

3.3.2.1. Fate of CuSe catalyst. Selenium has a distinct natural isotopic distribution made of six stable isotopes including ^{74}Se(0.89 %), ^{76}Se (9.37 %), ^{77}Se(7.63 %), ^{78}Se(23.77 %), ^{80}Se(49.61 %), and ^{82}Se(8.73 %), which can be detected in mass spectra by a unique isotope envelope pattern dictated by these masses. Having done experiments to evaluate whether Se species are distributed in solution, peaks centred around *m/z* 112, 113 and 129 were detected. These *m/z* values and the isotopic pattern surrounding them correspond to specific isotopic signatures of SeO$_2$, HSeO$_2$, and HSeO$_3^-$, respectively (Table S3 and Fig. S6 C&D). According to Fig. S6C, it is remarkable that the aqueous solutions that contained E1 and the catalyst showed strong signal patterns for SeO$_2$ (*) and HSeO$_3^-$ (^), while the solution of catalyst in water only (without E1) shows extremely low signal for these species (Fig. S6B). This suggests that these Se species are produced as a result of the adsorption of E1 on the catalyst surface. As expected, isotopic patterns of the Se species were not shown in E1 aqueous solution without a catalyst (Fig. S6A). Fig. S6D shows that after exposure of E1 solution to light in the presence of catalyst for 60 min, a new pattern of Se species centred around 113 (labelled +) appeared, which is assigned to HSeO$_2$ (Table S3 and Fig. S6D (+)). The change in peak areas for the most abundant *m/z* values 112, 113 and 129 corresponding to the species SeO$_2$, HSeO$_2^-$, and HSeO$_3^-$, respectively, were then plotted versus the reaction time (Fig. S7). During adsorption in the dark (i.e., the time from −30 min to 0 min for all experiments and up to 180 min for the experiments E1 + catalyst in dark, Fig. S7), peak areas of the three *m/z* values increased with time, indicating that these Se species were forming in solution at levels, according to their peak areas, in the order SeO$_2$ > HSeO$_3^-$ > HSeO$_2^-$.

To identify whether these Se species have contributed to the degradation of E1 in a homogeneous solution, samples were filtered after 30 min dark adsorption to remove the catalyst particles and were then exposed to light. As shown in Fig. S7 (*m/z* 269) (experiment: E1 + catalyst for 30 min then filtered), the change in peak area after filtration of the catalyst remained unchanged while the peak areas for the three Se species also remained unchanged with time (experiment: E1 + catalyst for 30 min then filtered) indicating that these species do not contribute to the oxidation of E1 in homogeneous solution (i.e., in the absence of the solid catalyst). However, in the co-presence of E1 and catalyst, the peak areas of the three Se species increased with time, with the increase being more significant under photocatalytic conditions (i.e., E1 + catalyst+light) than under dark conditions (i.e., E1 + catalyst in dark).

A possible mechanism for the formation of Se species would involve the formation of SeO_2 in the presence of oxygen in water which further aids the catalytic oxidation of E1. The surface oxidation of the catalyst has already been evidenced by XPS results (Fig. S2; and Section 3.1.1). Few studies on water splitting oxygen/hydrogen evolution reactions (OER/HER) have theorized that metal chalcogenides are prone to form an amorphous (oxy) hydroxide surface layer in the oxidative environment which upon oxidation leaches out the non-metal components such as Se, S, P, etc. (Wygant et al., 2018). The porous (oxy) layer formation is the leading cause of high photocatalytic performance of metal chalcogenides because it increases the surface area and provides enhanced active sites for catalytic activity (Jin, 2017; Noh et al., 2019; Wygant et al., 2018). SeO_2 will then oxidise E1 (Młochowski et al., 2003) to generate $Se(OH)_2$, which has an *m/z* 113 [M-H], while E1 gains an oxygen atom (i.e. *m/z* 285). Both *m/z* masses were detected in the mass spectrometry analysis, even during adsorption in the dark, which justifies the mechanism suggested. SeO_2 also hydrolyses to form H_2SeO_3 which is a di-acid with the pKa values 2.46 and 7.3. As the pH of the solution was around 6, dissociation of H_2SeO_3 to $HSeO_3$ should be the dominant species (Supplementary Information Fig. S8), which agrees with the mass spectrometry results (*m/z* 129). The equations representing these reactions are shown in Fig. 7.

3.3.2.2. Pathways of E1 oxidation. In photocatalysis, electron-hole pairs are formed on surface of the photocatalyst. Due to their lack of electrons, the valence band holes are powerful oxidants capable of attacking organic molecules either directly (i.e., electron transfer from the surface-bound substrate to the holes) or indirectly via formation of reactive oxygen species (ROS) such as hydroxyl radical ($^{\bullet}OH$), superoxide radical anion ($O_2^{\bullet-}$), or hydroperoxyl radical ($^{\bullet}OOH$) (Chong et al., 2010; Hoffmann et al., 1995). Amongst the reactive species formed, $^{\bullet}OH$ is the most potent radical that drives the oxidation reactions with rate constant values ranging from 10^8 to 10^{11} $M^{-1}s^{-1}$. It reacts according to three possible mechanisms including electron transfer, H-abstraction, and radical addition reaction (Buxton et al., 1988); electron-transfer reactions are uncommon. Since the activation energy for the hydrogen abstraction reaction is generally much higher than that for radical addition (Li et al., 2020), the preferred reaction mechanism is thus radical addition, which leads to the formation of hydroxylated molecules. When addition reactions are not favoured, due to steric hinderance for example, $^{\bullet}OH$ may also react by H-abstraction.

As E1 was degraded (Supplementary Information Fig. S7, *m/z* 269), the liquid mass spectrometry analysis revealed the formation of products with characteristic *m/z* values of 285, and 267, where their peak areas increased with the reaction time as shown in Fig. S8 (*m/z* 285 and 267, Supplementary Information). The *m/z* 285 represents an increase of 16 in molecular mass implying hydroxylation of E1 molecule with a loss of a hydrogen atom while the *m/z* 267 represents a loss of two hydrogen atoms from E1. According to the maximum values of Fukui index (f^o) for radical reactions, the preferable sites of radical attack are the carbon atoms of the hydroxylated aromatic ring at the positions, order of preference, $C_{18} > C_{19} > C_{17} > C_{20} > C_{16} > C_{14}$ (Supplementary Information Fig. S9). Similar results have also been obtained by other studies for the degradation of 17-β estradiol, which has a similar molecular
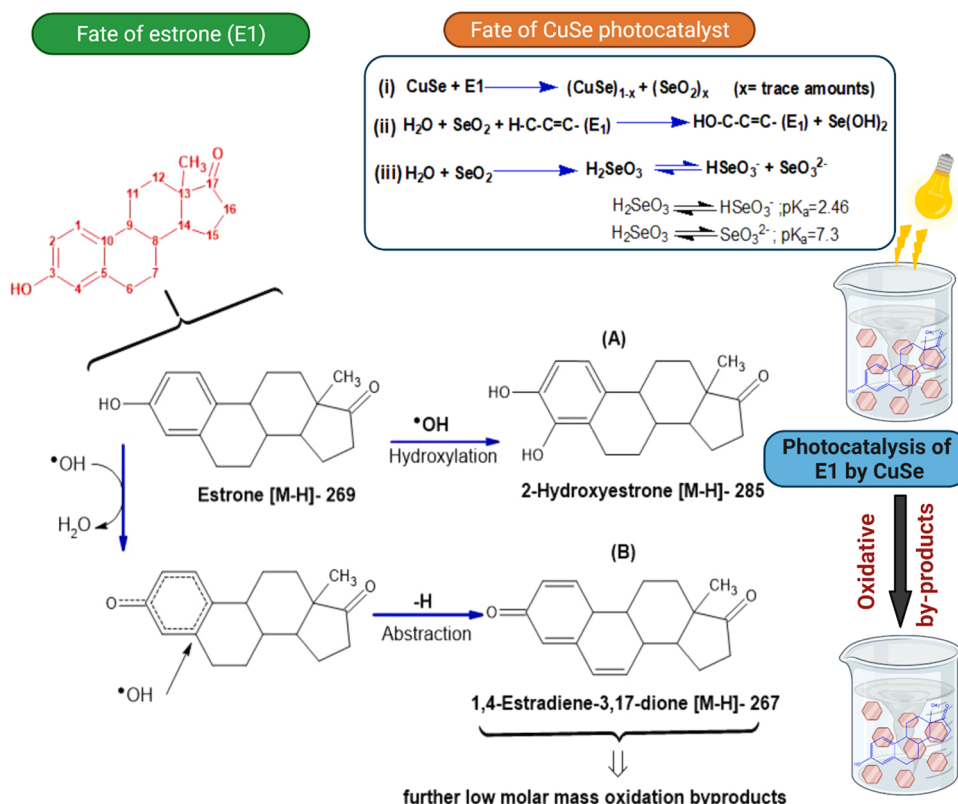

Fig. 7. Proposed E1 oxidation pathway by CuSe photocatalysis.

structure as E1 (Mai et al., 2008; Rokhina and Suri, 2012). Based on the computational and mass spectrometry analyses' results, a mechanism for E1 photocatalytic degradation by CuSe is suggested and is shown in Fig. 7.

The dispersion of CuSe in E1 aqueous solution triggers a series of catalytic redox reactions that are enhanced by visible-light irradiation, comprising primarily the formation of trace amounts of SeO_2 and $HSeO_3^-$ due to partially leaching out of the catalyst (Fig. 7 (reactions # i-iii) and as described in Section 3.3.2.1). The presence of ROS, in addition to selenium isotopic suspension (Fig. 7 (reaction ii)), expedites the
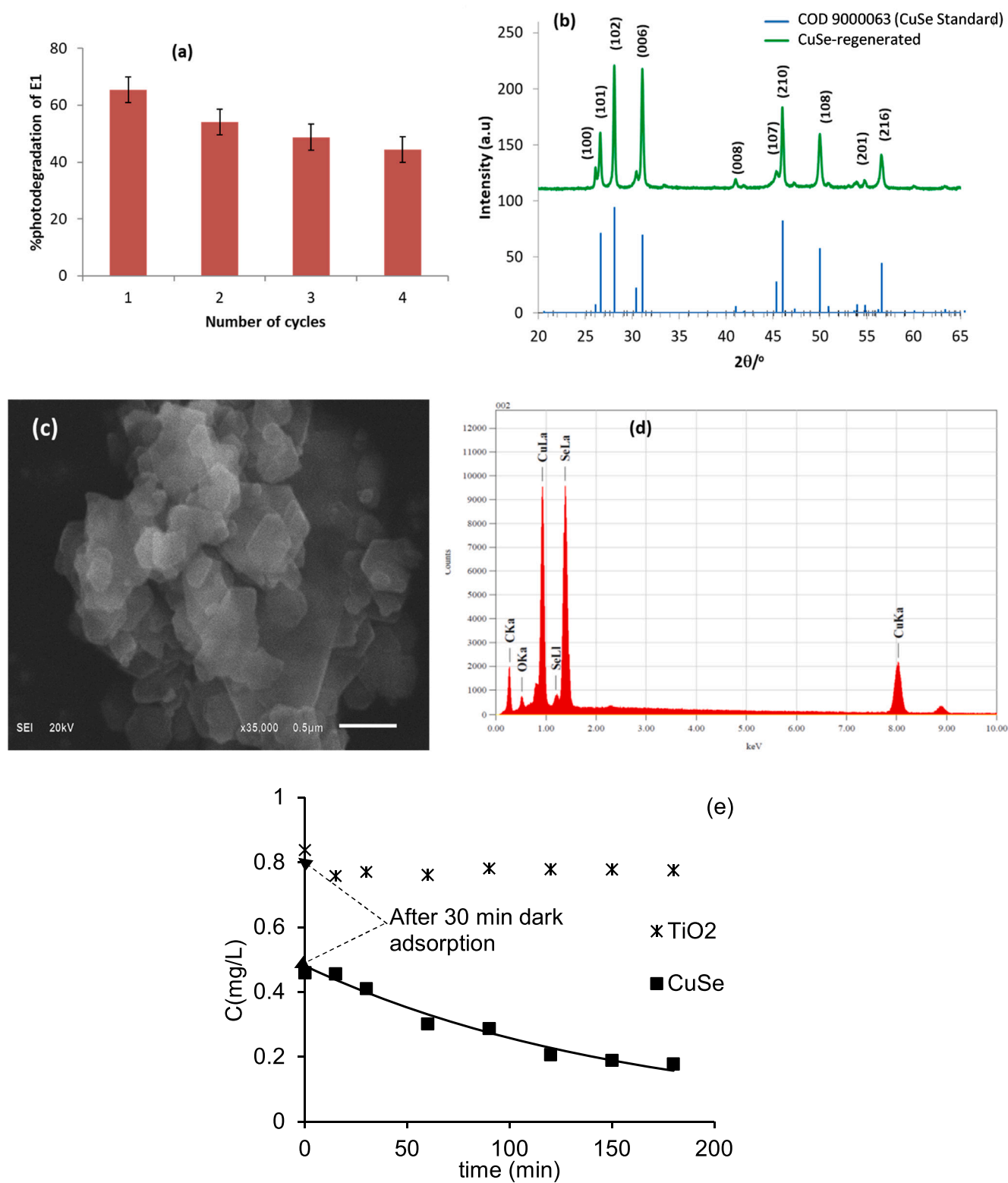
Fig. 8. **(a)** Recyclability of CuSe catalyst for photocatalytic degradation of E1 under visible-light irradiation for four consecutive cycles; **(b)** XRD of regenerated catalyst **(c)** SEM micrograph of regenerated catalyst; scale bar is 0.5 μm, **(d)** corresponding EDX elemental mapping and composition; **(e)** Comparison of photocatalytic degradation of E1 with CuSe and TiO_2 (P25).

hydroxylation of estrone into catechol estrone namely 2-hydroxyestrone (2-OHE1) shown in Fig. 7 as product A. The attack of E1 could also lead to the destabilization of the aromatic ring due to oxidation followed by the formation of another reaction by-product namely 1,4-estradiene-3,17-dione (product B in Fig. 7) (Ohe et al., 2000). These oxidative by-products are reported to have a less estrogenic effect than E1 (Pereira et al., 2011; Xu et al., 2021) which further decompose into low molecular weight intermediates upon extended photocatalytic degradation.

3.3.3. Catalyst recyclability and comparison with a benchmark photocatalyst (TiO2)

Generally, the practical applicability of a catalyst depends upon its economic feasibility which relies amongst other aspects on its recyclability efficiency. Therefore, we investigated the recyclability of the catalyst for E1 photodegradation for four cycles by observing its degradation extent. The catalyst was retrieved after each experiment that lasted for 60 min, washed with a mixture of ethanol and water

followed by vacuum drying and reused for four consecutive cycles. It was observed that the catalyst remained active in degrading E1 for four cycles, as illustrated by Fig. 8a, though with some reduction in degradation efficiency. Further, the regenerated catalyst was characterized for its structural properties to confirm its stability.

The corresponding XRD pattern, as shown in Fig. 8b, reveals that the crystal structure CuSe is retained after degradation. The diffraction peaks which include (100), (102), (006), (210), (108) are perfectly indexed and matched with the standard pattern (COD-9000063). The regenerated catalyst retained the hexagonal geometry of the crystallites as depicted in Fig. 8c. Additionally, the elemental mapping and chemical composition (Fig. 8d) authenticated the single-phase copper selenide structure. The sample was partly oxidized, as indicated by the presence of oxygen (Fig. 8d) due to the readily oxidizing nature of copper-containing compounds (Singh et al., 2018) besides, the sample synthesis and processing have taken place in the air. Similar observations are reported for the photocatalytic activity of Cu_2O by (Singh et al., 2018).

Table 1
A compilation of comparative studies of E1 photocatalytic degradation on a variety of photocatalysts.

Photocatalyst	Light source details (Type, power, wavelength)	Experimental conditions	Degradation kinetics	Reference
Zinc oxide (ZnO) BET surface area 10.7 m^2/g; particle size 100 nm–1 μm	Artificial ultraviolet (UVA) 18 W, (λ = 320–400 nm) with a peak intensity at 369 nm	C_0 = 0.6 mg/L V= 200 mL pH = 4	k_1 = 0.074 min^{-1} (0.01 g/L; t = 45 min, 95 % degradation) k_1 = 0.362 min^{-1} (0.5 g/L; t = 10 min; 95 % degradation)	(Han et al., 2012)
	Solar irradiation clear day from 13:00–13:30 local time (S36°51.179`; E174° 46.177`);		k_1 = 0.337 min^{-1} (0.05 g/L; t = 20 min; 99 % degradation)	
Degusa-titanium dioxide P25 BET surface area 48.6 m^2/g; Particle size 20–50 nm	Artificial ultraviolet (UVA)		k_1 = 0.036 min^{-1} (0.01 g/L; t = 60 min) k_1 = 0.177 min^{-1} (0.5 g/L; t = 25 min; 95 % degradation	
	solar irradiation		k_1 =0.328 min^{-1} (0.05 g/L; t = 20 min; 99 % degradation	
Immobilized porous titania sheets (50 mm diameter)	UV-LED, 1.67 mW; λ = 365 nm	C_0 = 0.004 mg/L; pH = 4	k_1 = 0.025 min^{-1} t = 120 min) 99.9 % degradation	(Arlos et al., 2016)
Ti coating on TiO2	UV-A HP mercury lamp, 125 W (λ = 315–400 nm)	C_0 = 0.01 mg/L	k_1 = 0.025 min^{-1} t = 60 min) 99.9 % degradation	(Coleman et al., 2004)
TiO2 film on quartz beads (d= 2 mm)	UVA, λ = 359 nm, Power not mentioned	C_0 = 0.1 mg/L	k_1 = 0.058 min^{-1} t = 30 min) 90 % degradation	(Tanizaki et al., 2002)
ZnO nanorod arrays (glass substrates of dimension 25 mm x 10 mm × 1 mm)	UVA, λ = 365 nm, Power not mentioned	C_0 = 0.5 mg/L	k_1 =not mentioned t = 360 min) 87 % degradation	(Liu et al., 2012)
TiO2-coated glass rings dimension 5 mm diameter and 2 mm length	(UVC & UVA lamps, 125 W	C_0 = 0.02 mg/L V= 150 mL pH =7	k_1 =not mentioned t = 60 min) 90 % degradation	(Liz et al., 2018)
Degussa P-25 TiO2 powder suspension		dosage=0.2 g/L	k_1 =not mentioned t = 60 min) 98 % degradation	
Cu_2O nano-cubes (Particle size 20–30 nm)	Xe lamp (150 W)	C_0 = 40 mg/L V= 40 mL Dosage= 0.04 g/L pH 7	k_1 = 0.032 min^{-1} t = 45 min) 97 % degradation	(Mukherjee et al., 2017)
Cu_2O nano-octahedra (Particle size 70–96 nm)			k_1 = 0.035 min^{-1} t = 45 min) 90 % degradation	
Cu_2O nano-rods (Particle size 80–112 nm)			k_1 = 0.05 min^{-1} t = 60 min) 92 % degradation	
CuSe hexagonal nanoflakes (average particle size and thickness of 0.229 ± 0.146 μm and 0.05 ± 0.02 μm)	Hg-Xe lamp (60 W) λ = 300–700 nm	C_0 = 1 mg/L V= 100 mL Dosage= 0.5 g/L pH 7	adsorption kinetics q_e= 1.44 mg/g k_1 = 0.037 min^{-1} t = 30 min Photocatalytic kinetics: k_1 = 0.013 min^{-1} t = 90 min) > 90 % degradation	This study

t: time required for E1 decomposition
k_1: first-order rate constant
V: volume of the solution
C_0: initial concentration of E1
q_e: Equilibrium adsorbent uptake concentration

Furthermore, TiO_2 photocatalyst has widely been employed for photocatalytic degradation of estrogenic compounds and is profoundly considered as a benchmark for their treatment despite having a wide bandgap, as shown in Table 1. A compilation of photocatalytic degradation studies of estrone on a variety of photocatalysts is presented in Table 1, where the remarkable performance of CuSe is observed. A detailed insight into these listed studies manifests that the E1 photocatalytic degradation phenomenon has been, however, inadequately investigated so far. The oxidative reaction pathways and reaction by-products of E1 decomposition have been briefly discussed in a few studies. Overall, visible-light-induced E1 photocatalytic degradation is barely investigated to date, which reveals a knowledge gap to be addressed. Nevertheless, CuSe exhibited remarkable degradation of E1 up to 90 % by combining adsorption, oxidation, and visible-light-driven photocatalysis. To validate and pursue the efficacy of our synthesized CuSe catalyst, we compared the extent of photocatalytic degradation of the CuSe catalyst with the benchmark TiO_2 (P25) photocatalyst under the same light source, as presented in Fig. 8e. Interestingly, the CuSe catalyst has shown remarkable enhancement in both dark-adsorption and photodegradation efficiencies of E1 compared to TiO_2 photocatalyst under similar conditions. The removal of E1 after 30 min of adsorption in dark by CuSe was 54 % which is significantly higher than that by TiO_2 (only 16 %). Upon exposure to light for 180 min, the overall removal of E1 was 82 % by CuSe but only 22 % by TiO_2.

These findings imply that having visible-light activation as well as oxidation abilities, CuSe could serve as a better option for photocatalytic degradation of estrone in water. In addition, these experimental findings have ascertained the novelty of the as-synthesized CuSe photocatalyst, which could be an ideal candidate for the remediation of estrogenic pollution and can further be employed for the treatment of related endocrine disruptors and pharmaceuticals in water.

4. Conclusion

In this study, visible-light-induced photocatalytic degradation of estrone (E1) by copper selenide (CuSe) nanocrystals was targeted. E1 was not only selected owing to its potent toxicity but also because of its persistent nature and wide abundance. We have successfully synthesized hexagonal copper selenide (CuSe) nanoflakes by a facile and low-temperature modified co-precipitation method. CuSe nanocrystals having flakes-like morphology with a bandgap of 1.60 eV exhibited remarkable degradation of E1 up to 90 % by combining adsorption, oxidation, and visible-light-driven photocatalysis. The catalyst has shown enhanced photodegradation in comparison to the benchmark TiO_2 (P25) due to the combined effects it presents and photocatalysis under visible-light irradiation. Based on the computational and mass spectrometry analyses, a mechanism for E1 shows that E1 oxidation is accompanied by oxygen addition and hydrogen abstraction. Moreover, the synthesized catalyst could be economically feasible since it showed efficient visible-light activity and enhanced removal of estrone. Therefore, these findings might prove instrumental in exploring the potential of hexagonal CuSe photocatalysts in a wide range of pollution remediation challenges.

Declaration of Competing Interest

The authors declare that they have no known competing financial interests or personal relationships that could have appeared to influence the work reported in this paper.

Acknowledgements

Appendix A. Supporting information

References

Acedo-Mendoza, A., Infantes-Molina, A., Vargas-Hernández, D., Chávez-Sánchez, C., Rodríguez-Castellón, E., Tánori-Córdova, J., 2020. Photodegradation of methylene blue and methyl orange with CuO supported on ZnO photocatalysts: the effect of copper loading and reaction temperature. Mater. Sci. Semicond. Process. 119, 105257 https://doi.org/10.1016/j.mssp.2020.105257.

Adeel, M., Song, X., Wang, Y., Francis, D., Yang, Y., 2017. Environmental impact of estrogens on human, animal and plant life: a critical review. Environ. Int. 99, 107–119. https://doi.org/10.1016/j.envint.2016.12.010.

Ali, A., Cung Tien Nguyen, D., Cho, K.-Y., Oh, W.-C., 2018. A simple ultrasonic-synthetic route of Cu2Se-graphene-TiO2 ternary composites for carbon dioxide conversion processes. Fullerenes. Nanotub. Carbon Nanostruct. 26, 827–836. https://doi.org/10.1080/1536383X.2018.1504211.

Amin, M.M., Bina, B., Ebrahimi, A., Yavari, Z., Mohammadi, F., Rahimi, S., 2018. The occurrence, fate, and distribution of natural and synthetic hormones in different types of wastewater treatment plants in Iran. Chin. J. Chem. Eng. 26, 1132–1139. https://doi.org/10.1016/j.cjche.2017.09.005.

Arguello-Pérez, M.Á., Mendoza-Pérez, J.A., Tintos-Gómez, A., Ramírez-Ayala, E., Godínez-Domínguez, E., Silva-Bátiz, F.D.A., 2019. Ecotoxicological analysis of emerging contaminants from wastewater discharges in the Coastal Zone of Cihuatlán (Jalisco, Mexico). Water 11, 1386. https://doi.org/10.3390/w11071386.

Arlos, M.J., Liang, R., Hatat-Fraile, M.M., Bragg, L.M., Zhou, N.Y., Servos, M.R., Andrews, S.A., 2016. Photocatalytic decomposition of selected estrogens and their estrogenic activity by UV-LED irradiated TiO2 immobilized on porous titanium sheets via thermal-chemical oxidation. J. Hazard. Mater. 318, 541–550. https://doi.org/10.1016/j.jhazmat.2016.07.048.

Bloh, J.Z., 2019. A holistic approach to model the kinetics of photocatalytic reactions. Front. Chem. 7, 128. https://doi.org/10.3389/fchem.2019.00128.

Buxton, G.V., Greenstock, C.L., Helman, W.P., Ross, A.B., 1988. Critical review of rate constants for reactions of hydrated electrons, hydrogen atoms and hydroxyl radicals (· OH/· O− in aqueous solution. J. Phys. Chem. Ref. Data 17, 513–886. https://doi.org/10.1063/1.555805.

Cai, J., Zhu, Y., Xie, S., Niu, B., Zhang, Y.-N., Li, L., Li, D., Zhao, G., 2021. Accurate removal of trace 17β-estradiol and estrogenic activity in blended systems under a photoelectrocatalytic circulating flow. Environ. Sci. Technol. 55, 12585–12595. https://doi.org/10.1021/acs.est.1c02630.

Chakraborty, B., Beltrán-Suito, R., Hlukhyy, V., Schmidt, J., Menezes, P.W., Driess, M., 2020. Crystalline copper selenide as a reliable non-noble electro (pre) catalyst for overall water splitting. ChemSusChem 13, 3222–3229. https://doi.org/10.1002/cssc.202000445.

Chen, S., Ma, G., Wang, Q., Sun, S., Hisatomi, T., Higashi, T., Wang, Z., Nakabayashi, M., Shibata, N., Pan, Z., 2019. Metal selenide photocatalysts for visible-light-driven Z-scheme pure water splitting. J. Mater. Chem. A7, 7415–7422. https://doi.org/10.1039/C9TA00768G.

Chong, M.N., Jin, B., Chow, C.W., Saint, C., 2010. Recent developments in photocatalytic water treatment technology: a review. Water Res. 44, 2997–3027. https://doi.org/10.1016/j.watres.2010.02.039.

Coleman, H., Routledge, E., Sumpter, J., Eggins, B., Byrne, J., 2004. Rapid loss of estrogenicity of steroid estrogens by UVA photolysis and photocatalysis over an immobilised titanium dioxide catalyst. Water Res. 38, 3233–3240. https://doi.org/10.1016/j.watres.2004.04.021.

Coleman, H.M., Eggins, B.R., Byrne, J.A., Palmer, F.L., King, E., 2000. Photocatalytic degradation of 17-β-oestradiol on immobilised TiO2. Appl. Catal. B: Environ. 24, L1–L5. https://doi.org/10.1016/S0926-3373(99)00091-0.

Criddle, A.J., Stanley, C.J., 2012. Quantitative data file for ore minerals. & Business Media. Springer Science,. https://doi.org/10.1007/978-94-011-1486-8.

Dwinandha, D., Zhang, B., Fujii, M., 2022. Prediction of reaction mechanism for OH radical-mediated phenol oxidation using quantum chemical calculation. Chemosphere 291, 132763. https://doi.org/10.1016/j.chemosphere.2021.132763.

Elias, K.D., Ejidike, I.P., Mtunzi, F.M., Pakade, V.E., 2021. Endocrine disruptors-(estrone and β-estradiol) removal from water by nutshell activated carbon: kinetic, isotherms and thermodynamic studies. Chem. Thermodyn. Therm. Anal. 3, 100013 https://doi.org/10.1016/j.ctta.2021.100013.

Fredj, S.B., Nobbs, J., Tizaoui, C., Monser, L., 2015. Removal of estrone (E1), 17β-estradiol (E2), and 17α-ethinylestradiol (EE2) from wastewater by liquid–liquid extraction. Chem. Eng. J. 262, 417–426. https://doi.org/10.1016/j.cej.2014.10.007.

Gabet, A., Métivier, H., De Brauer, C., Mailhot, G., Brigante, M., 2021. Hydrogen peroxide and persulfate activation using UVA-UVB radiation: degradation of

estrogenic compounds and application in sewage treatment plant waters. J. Hazard. Mater. 405, 124693 https://doi.org/10.1016/j.jhazmat.2020.124693.

Gao, F., Zhu, L., Wang, Y., Xie, H., Li, J., 2016. Room temperature facile synthesis of Cu2Se hexagonal nanoplates array film and its high photodegradation activity to methyl blue with the assistance of H2O2. Mater. Lett. 183, 425–428. https://doi.org/10.1016/j.matlet.2016.07.155.

Ghosh, A., Kulsi, C., Banerjee, D., Mondal, A., 2016. Galvanic synthesis of Cu2− xSe thin films and their photocatalytic and thermoelectric properties. Appl. Surf. Sci. 369, 525–534. https://doi.org/10.1016/j.apsusc.2016.02.020.

Han, J., Liu, Y., Singhal, N., Wang, L., Gao, W., 2012. Comparative photocatalytic degradation of estrone in water by ZnO and TiO2 under artificial UVA and solar irradiation. Chem. Eng. J. 213, 150–162. https://doi.org/10.1016/j.cej.2012.09.066.

Hoffmann, M.R., Martin, S.T., Choi, W., Bahnemann, D.W., 1995. Environmental applications of semiconductor photocatalysis. Chem. Rev. 95, 69–96. https://doi.org/10.1021/cr00033a004.

Honorio, J.F., Veit, M.T., Suzaki, P.Y.R., Coldebella, P.F., Rigobello, E.S., Tavares, C.R.G., 2018. Adsorption of naturals hormones estrone, 17β-estradiol, and estriol by rice husk: monocomponent and multicomponent kinetics and equilibrium. Environ. Technol. https://doi.org/10.1080/09593330.2018.1521472.

Hurwitz, A., Liu, S., T., 1977. Determination of aqueous solubility and pKa values of estrogens. J. Pharm. Sci. 66, 624–627. https://doi.org/10.1002/jps.2600660504.

Iqbal, M., Bhatti, H.N., Younis, S., Rehmat, S., Alwadai, N., Almuqrin, A.H., Iqbal, M., 2021. Graphene oxide nanocomposite with CuSe and photocatalytic removal of methyl green dye under visible light irradiation. Diam. Relat. Mater. 113, 108254 https://doi.org/10.1016/j.diamond.2021.108254.

Jin, S., 2017. Are metal chalcogenides, nitrides, and phosphides oxygen evolution catalysts or bifunctional catalysts? ACS Energy Letters. ACS Publications. https://doi.org/10.1021/acsenergylett.7b00679.

Karthik, K., Raghu, A., Reddy, K.R., Ravishankar, R., Sangeeta, M., Shetti, N.P., Reddy, C. V., 2022. Green synthesis of Cu-doped ZnO nanoparticles and its application for the photocatalytic degradation of hazardous organic pollutants. Chemosphere 287, 132081. https://doi.org/10.1016/j.chemosphere.2021.132081.

Kevorkyants, R., Farooq, S., Tizaoui, C., 2022. Crystal and electronic structure of the substoichiometric photocatalyst Cu4Se6: DFT study. J. Phys. Chem. Solids 162, 110529. https://doi.org/10.1016/j.jpcs.2021.110529.

Kumar, A., Pandey, G., 2017. A review on the factors affecting the photocatalytic degradation of hazardous materials. Mater. Sci. Eng. Int. J. 1, 1–10. https://doi.org/10.15406/mseij.2017.01.00018.

Li, H., Miao, X., Zhang, J., Du, J., Xu, S., Tang, J., Zhang, Y., 2020. DFT studies on the reaction mechanism and kinetics of dibutyl phthalate initiated by hydroxyl and sulfate radicals: prediction of the most reactive sites. Chem. Eng. J. 381, 122680 https://doi.org/10.1016/j.cej.2019.122680.

Lian, L., Miao, C., Hao, Z., Liu, Q., Liu, Y., Song, W., Yan, S., 2021. Reevaluation of the contributions of reactive intermediates to the photochemical transformation of 17β-estradiol in sewage effluent. Water Res. 189, 116633.

Liu, M.L., Chen, B.B., Li, R.S., Li, C.M., Zou, H.Y., Huang, C.Z., 2017. Dendritic CuSe with hierarchical side-branches: synthesis, efficient adsorption, and enhanced photocatalytic activities under daylight. *ACS Sustain. Chem. Eng.* 5, 4154–4160. https://doi.org/10.1021/acssuschemeng.7b00126.

Liu, S., Rong, C., Lu, T., 2014a. Information conservation principle determines electrophilicity, nucleophilicity, and regioselectivity. J. Phys. Chem. A 118, 3698–3704. https://doi.org/10.1021/jp5032702.

Liu, X., Duan, X., Peng, P., Zheng, W., 2011. Hydrothermal synthesis of copper selenides with controllable phases and morphologies from an ionic liquid precursor. Nanoscale 3, 5090–5095. https://doi.org/10.1039/C1NR10833F.

Liu, Y., Han, J., Qiu, W., Gao, W., 2012. Hydrogen peroxide generation and photocatalytic degradation of estrone by microstructural controlled ZnO nanorod arrays. Appl. Surf. Sci. 263, 389–396. https://doi.org/10.1016/j.apsusc.2012.09.067.

Liu, Y.-Q., Wang, F.-X., Xiao, Y., Peng, H.-D., Zhong, H.-J., Liu, Z.-H., Pan, G.-B., 2014b. Facile microwave-assisted synthesis of klockmannite CuSe nanosheets and their exceptional electrical properties. Sci. Rep. 4, 1–8. https://doi.org/10.1038/srep05998.

Liu, Y.-Q., Wu, H.-D., Zhao, Y., Pan, G.-B., 2015. Metal ions mediated morphology and phase transformation of chalcogenide semiconductor: from CuClSe2 microribbon to CuSe nanosheet. Langmuir 31, 4958–4963. https://doi.org/10.1021/acs.langmuir.5b00373.

Liz, M.V.D., Lima, R.M.D., Amaral, B.D., Marinho, B.A., Schneider, J.T., Nagata, N., Peralta-Zamora, P., 2018. Suspended and immobilized TiO 2 photocatalytic degradation of estrogens: potential for application in wastewater treatment processes. J. Braz. Chem. Soc. 29, 380–389. https://doi.org/10.21577/0103-5053.20170151.

Lu, T., Chen, F.J., 2012. Multiwfn: a multifunctional wavefunction analyzer. J. Comput. Chem. 33, 580–592. https://doi.org/10.1002/jcc.22885.

Mai, J., Sun, W., Xiong, L., Liu, Y., Ni, J., 2008. Titanium dioxide mediated photocatalytic degradation of 17β-estradiol in aqueous solution. Chemosphere 73, 600–606. https://doi.org/10.1016/j.chemosphere.2008.05.073.

Mills, A., O'rourke, C., Moore, K., 2015. Powder semiconductor photocatalysis in aqueous solution: An overview of kinetics-based reaction mechanisms. J. Photochem. Photobiol. A: Chem. 310, 66–105. https://doi.org/10.1016/j.jphotochem.2015.04.011.

Mkhalid, I., 2016. Visible light photocatalytic degradation of 2-chlorophenol in wastewater using copper selenide nanorods. Nanosci. Nanotechnol. Lett. 8, 744–749. https://doi.org/10.1166/nnl.2016.2248.

Młochowski, J., Brząszcz, M., Giurg, M., Palus, J., Wójtowicz, H., 2003. Selenium-promoted oxidation of organic compounds: Reactions and mechanisms. Eur. J. Org. Chem. 2003, 4329–4339. https://doi.org/10.1002/ejoc.200300230.

Mukherjee, I., Mishrra, A., Saha, R., Chatterjee, S., 2017. Efficient degradation of endocrine disruptors using 1D and 3D copper (I) oxide nanostructures. ChemistrySelect 2, 6388–6398. https://doi.org/10.1002/slct.201701181.

Murtada, K., Salghi, R., Ríos, A., Zougagh, M., 2020. A sensitive electrochemical sensor based on aluminium doped copper selenide nanoparticles-modified screen printed carbon electrode for determination of L-tyrosine in pharmaceutical samples. J. Electroanal. Chem. 874, 114466 https://doi.org/10.1016/j.jelechem.2020.114466.

Naumkin, A.V., Kraut-Vass, A., Gaarenstroom, S.W., Powell, C.J., Gaithersburg, T., 2012. NIST X-ray photoelectron spectroscopy database, version 4.1, p. 1.

Noh, H., Yang, Y., Ahn, S., Peters, A.W., Farha, O.K., Hupp, J.T., 2019. Molybdenum sulfide within a metal–organic framework for photocatalytic hydrogen evolution from water. J. Electrochem. Soc. 166, H3154. https://doi.org/10.1149/2.0261905jes.

Ohe, T., Hirobe, M., Mashino, T., 2000. Novel metabolic pathway of estrone and 17β-estradiol catalyzed by cytochrome P-450. Drug Metab. Dispos. 28, 110–112. ⟨http://dmd.aspetjournals.org/⟩.

O'shea, K.E., Cardona, C., 1995. The reactivity of phenol in irradiated aqueous suspensions of TiO2. Mechanistic changes as a function of solution pH. J. Photochem. Photobiol. A: Chem. 91, 67–72. https://doi.org/10.1016/1010-6030(95)04103-M.

Peiris, S.M., Pearson, T.T., Heinz, D.L., 1998. Compression of klockmannite, CuSe. J. Chem. Phys. 109, 634–636. https://doi.org/10.1063/1.476601.

Pereira, R.O., Postigo, C., De Alda, M.L., Daniel, L.A., Barceló, D., 2011. Removal of estrogens through water disinfection processes and formation of by-products. Chemosphere 82, 789–799. https://doi.org/10.1016/j.chemosphere.2010.10.082.

Perondi, T., Michelon, W., Junior, P.R., Knoblauch, P.M., Chiareloto, M., De Fátima Peralta Muniz Moreira, R., Peralta, R.A., Düsman, E., Pokrywiecki, T.S., 2020. Advanced oxidative processes in the degradation of 17β-estradiol present on surface waters: kinetics, byproducts and ecotoxicity. Environ. Sci. Pollut. Res. 27, 21032–21039. https://doi.org/10.1007/s11356-020-08618-2.

Pratush, A., Ye, X., Yang, Q., Kan, J., Peng, T., Wang, H., Huang, T., Xiong, G., Hu, Z., 2020. Biotransformation strategies for steroid estrogen and androgen pollution. Appl. Microbiol. Biotechnol. 104, 2385–2409. https://doi.org/10.1007/s00253-020-10374-9.

Prokić, D., Vukčević, M., Mitrović, A., Maletić, M., Kalijadis, A., Janković-Častvan, I., Đurkić, T., 2022. Adsorption of estrone, 17β-estradiol, and 17α-ethinylestradiol from water onto modified multi-walled carbon nanotubes, carbon cryogel, and carbonized hydrothermal carbon. Environ. Sci. Pollut. Res. 29, 4431–4445. https://doi.org/10.1007/s11356-021-15970-4.

Puma, G.L., Puddu, V., Tsang, H.K., Gora, A., Toepfer, B., 2010. Photocatalytic oxidation of multicomponent mixtures of estrogens (estrone (E1), 17β-estradiol (E2), 17α-ethynylestradiol (EE2) and estriol (E3)) under UVA and UVC radiation: Photon absorption, quantum yields and rate constants independent of photon absorption. Appl. Catal. B: Environ. 99, 388–397. https://doi.org/10.1016/j.apcatb.2010.05.015.

Qin, F., Wan, T., Qiu, J., Wang, Y., Xiao, B., Huang, Z., 2020. Temperature effects on photocatalytic heat changes and kinetics via in situ photocalorimetry-fluorescence spectroscopy. Acta Phys. -Chim. Sin. 36. https://doi.org/10.3866/PKU.WHXB201905087.

Reddy, C.V., Koutavarapu, R., Reddy, K.R., Shetti, N.P., Aminabhavi, T.M., Shim, J., 2020. Z-scheme binary 1D ZnWO4 nanorods decorated 2D NiFe2O4 nanoplates as photocatalysts for high efficiency photocatalytic degradation of toxic organic pollutants from wastewater. J. Environ. Manag. 268, 110677 https://doi.org/10.1016/j.jenvman.2020.110677.

Riha, S.C., Johnson, D.C., Prieto, A.L., 2011. Cu2Se nanoparticles with tunable electronic properties due to a controlled solid-state phase transition driven by copper oxidation and cationic conduction. J. Am. Chem. Soc. 133, 1383–1390. https://doi.org/10.1021/ja106254h.

Rokhina, E.V., Suri, R.P., 2012. Application of density functional theory (DFT) to study the properties and degradation of natural estrogen hormones with chemical oxidizers. Sci. Total Environ. 417, 280–290. https://doi.org/10.1016/j.scitotenv.2011.12.008.

Schaefer, T., Wen, L., Estelmann, A., Maak, J., Herrmann, H., 2020. pH-and temperature-dependent kinetics of the oxidation reactions of OH with succinic and pimelic acid in aqueous solution. Atmosphere 11, 320. https://doi.org/10.3390/atmos11040320.

Shi, W., Shi, J., Yu, S., Liu, P., 2013. Ion-exchange synthesis and enhanced visible-light photocatalytic activities of CuSe-ZnSe flower-like nanocomposites. Appl. Catal. B: Environ. 138, 184–190. https://doi.org/10.1016/j.apcatb.2013.02.031.

Singh, M., Jampaiah, D., Kandjani, A.E., Sabri, Y.M., Della Gaspera, E., Reineck, P., Judd, M., Langley, J., Cox, N., Van Embden, J., 2018. Oxygen-deficient photostable Cu 2 O for enhanced visible light photocatalytic activity. Nanoscale 10, 6039–6050. https://doi.org/10.1039/C7NR08388B.

Srinivas, M., Venkata, R.C., Kakarla, R.R., Shetti, N.P., Reddy, M., Anjanapura, V.R., 2019. Novel Co and Ni metal nanostructures as efficient photocatalysts for photodegradation of organic dyes. Mater. Res. Express 6, 125502. https://doi.org/10.1088/2053-1591/ab5328.

Tang, Z., Liu, Z.-H., Wang, H., Dang, Z., Yin, H., Zhou, Y., Liu, Y., 2020. Trace determination of eleven natural estrogens and insights from their occurrence in a municipal wastewater treatment plant and river water. Water Res. 182, 115976 https://doi.org/10.1016/j.watres.2020.115976.

Tanizaki, T., Kadokami, K., Shinohara, R., 2002. Catalytic photodegradation of endocrine disrupting chemicals using titanium dioxide photosemiconductor thin films. Bull. Environ. Contam. Toxicol. 68, 732–739. https://doi.org/10.1007/s001280315.

Turchi, C.S., Ollis, D.F., 1990. Photocatalytic degradation of organic water contaminants: mechanisms involving hydroxyl radical attack. J. Catal. 122, 178–192. https://doi.org/10.1016/0021-9517(90)90269-P.

Vo, Q.V., Hoa, N.T., Mechler, A., 2021. Another look at reactions of 4-hydroxycoumarin with hydroxyl radical in the environment: deprotonation and diffusion effects. N. J. Chem. 45, 17683–17691. https://doi.org/10.1039/D1NJ03557F.

Wang, J., Ji, H., Lai, J., Yuan, R., Zheng, X., Liu, H., Jin, Z., 2016. Oriented klockmannite CuSe nanoplates: polyol solution synthesis and its application on a inorganic–organic hybrid photodetector. Cryst. Growth Des. 16, 6250–6262. https://doi.org/10.1021/acs.cgd.6b00734.

Wang, Y., Zhukovskyi, M., Tongying, P., Tian, Y., Kuno, M., 2014. Synthesis of ultrathin and thickness-controlled Cu2–x Se nanosheets via cation exchange. J. Phys. Chem. Lett. 5, 3608–3613. https://doi.org/10.1021/jz5019288.

Weizel, A., Schlüsener, M.P., Dierkes, G., Wick, A., Ternes, T.A., 2021. Fate and behavior of progestogens in activated sludge treatment: Kinetics and transformation products. Water Res. 188, 116515 https://doi.org/10.1016/j.watres.2020.116515.

Wilcox, J., 2012. Carbon capture. Springer Science & Business Media. https://doi.org/10.1007/978-1-4614-2215-0.

Wygant, B.R., Kawashima, K., Mullins, C.B., 2018. Catalyst or precatalyst? The effect of oxidation on transition metal carbide, pnictide, and chalcogenide oxygen evolution catalysts. ACS Energy Lett. 3, 2956–2966. https://doi.org/10.1021/acsenergylett.8b01774.

Xu, J., Yang, Q., Kang, W., Huang, X., Wu, C., Wang, L., Luo, L., Zhang, W., Lee, C.S., 2015. Water evaporation induced conversion of CuSe nanoflakes to Cu2– xSe

hierarchical columnar superstructures for high-performance solar cell applications. Part. Part. Syst. Charact. 32, 840–847. https://doi.org/10.1002/ppsc.201400253.

Xu, S., Sun, J., Zhang, Y., Ji, J., Sun, X.E., Safety, E., 2021. Opposite estrogen effects of estrone and 2-hydroxyestrone on MCF-7 sensitivity to the cytotoxic action of cell growth, oxidative stress and inflammation activity. Ecotoxicol. Environ. Saf. 209, 111754 https://doi.org/10.1016/j.ecoenv.2020.111754.

Yang, C.-T., Hsiang, H.-I., 2018a. Rapid synthesis and characterization of nearly dispersed marcasite CuSe2 and berzelianite Cu2Se crystallites using the chemical reduction process. Mater. Res. Bull. 97, 30–36. https://doi.org/10.1016/j.materresbull.2017.08.052.

Yang, C.-T., Hsiang, H.-I., 2018b. Rapid synthesis and characterization of nearly dispersed marcasite CuSe2 and berzelianite Cu2Se crystallites using the chemical reduction process. Mater. Res. Bull. 97, 30–36.

Yasir, M., Šopík, T., Lovecká, L., Kimmer, D., Sedlařík, V., 2021. The adsorption, kinetics, and interaction mechanisms of various types of estrogen on electrospun polymeric nanofiber membranes. Nanotechnology 33, 075702. https://doi.org/10.1088/1361-6528/ac357b.

Zhang, A., Ma, Q., Wang, Z., Lu, M., Yang, P., Zhou, G., 2010. Controllable synthesis of copper selenide nanocrystals through a green paraffin-acetate method. Mater. Chem. 124, 916–921. https://doi.org/10.1016/j.matchemphys.2010.08.044.

Zhang, J., Yu, J., Zhang, Y., Li, Q., Gong, J.R., 2011. Visible light photocatalytic H2-production activity of CuS/ZnS porous nanosheets based on photoinduced interfacial charge transfer. Nano Lett. 11, 4774–4779. https://doi.org/10.1021/nl202587b.

Zhang, Q., Xue, C., Owens, G., Chen, Z., 2022. Isolation and identification of 17β-estradiol degrading bacteria and its degradation pathway. J. Hazard. Mater. 423, 127185 https://doi.org/10.1016/j.jhazmat.2021.127185.